MSc Thesis

Co/CNT Fischer-Tropsch Catalysts

Influence of surface functionalization and impregnation solvent on structure and performance

Wouter Lamme BSc

February 2014

Supervisors
Dipl.-Chem. Thomas Eschemann
Prof.dr.ir. Krijn de Jong

Inorganic Chemistry and Catalysis
Debye Institute for Nanomaterials Science
Utrecht University

Universiteit Utrecht

Table of Contents

Chapter 1

Introduction

After the 1920s discovery of the Fischer-Tropsch process that converts a mixture of carbon monoxide and hydrogen to hydrocarbons, interest in Fischer-Tropsch technology as an alternative source of fuels has been in spurts, driven by wars, political situations and fluctuating oil price and availability [1], [2].

This chapter covers the history and relevance of the Fischer-Tropsch synthesis (Section 1.1), gives an introduction to the Fischer-Tropsch process (Section 1.2) and describes carbon nanotubes as a potential support for cobalt-based Fischer-Tropsch catalysts (Section 1.3). The last section will describe the scope of this thesis.

1.1 History and relevance of the Fischer-Tropsch synthesis

In the 1920s, the Germans Franz Fischer and Hans Tropsch reported about a catalytic process to convert a mixture of carbon monoxide and hydrogen (synthesis gas or syngas) into hydrocarbons. The main development took place at the Kaiser Wilhelm Institute for Coal Research (presently Max Plank Institute) in Mülheim (Ruhr) in collaboration with Ruhrchemie [3]. Just before World War II, by 1938, nine Fischer-Tropsch synthesis (FTS) plants in Germany had a combined capacity of 591 kt/y [4], roughly equal to 12,000 bbl/d [5]. The plants were built in an attempt to overcome shortages resulting from import restrictions during the war and were used to produce fuel, lubricants and fatty acids [6], [7]. The process was cobalt catalyzed and used syngas produced from coal. The plants were responsible for the production of a significant part of the gasoline used in Germany during World War II: in 1943, the annual gasoline production by the FT process reached the notable amount of 368,000 metric tons [8]. In May 1944 the allies started bombing synthetic oil plants resulting in a reduction in monthly production from 316,000 metric tons when the attacks began to 17,000 metric tons in September 1944. The facilities were recovered somewhat but until the end of the war, production remained a fraction of the pre-attack output [9]. After the war, operation of the FTS plants in West Germany stopped and some plants in East Germany were confiscated by the Soviet Union. Research and development continued in the United States, the United Kingdom and West Germany. In the 1950s, the price of natural gas increased causing a 360 kt/y plant in Brownsville, TX, USA using syngas obtained from natu-

ral gas to be closed and the research and development on the FTS decreased [2], [8], [10], except for South Africa: from the 1950s South Africa built coal-to-liquid (CTL) plants through which oil independence was guaranteed during apartheid. South African Synthetic Oil Limited (SASOL) is still producing CTL fuels. From the 1970s onwards FT research has regained interest [11].

As is the case for most countries, Germany and South Africa do not possess sufficient oil resources and are thus dependent on other countries. However, both countries do possess large amounts of coal and by using the Fischer-Tropsch process to convert coal into liquids the countries circumvented this dependency for fuel supply. More recently, in 2009, Russia shut off natural gas supply to Ukraine in a price conflict [12]. The need for a stable and independent fuel supply is obvious (although both Germany and The Netherlands have decided to stop coal mining [13], [14]).

The syngas used by Germany and South Africa was produced from coal. The conversion of coal via the Fischer-Tropsch synthesis is abbreviated as coal to liquid, or CTL. Syngas can also be obtained from feedstocks other than coal, e.g. natural gas for gas to liquid (GTL), biomass for biomass to liquid (BTL) and waste [15]. The general term for conversion of any feedstock to liquids via FTS or other methods is anything to liquid (XTL).

Driving forces for the Fischer-Tropsch process are not just geopolitical. It has been calculated before (2005) that Fischer-Tropsch alternatives to oil become economically competitive when oil prices rise above a certain amount [16]. **Figure 1.1** illustrates the oil price has been higher from 1974 to 1985 and since 2004 for GTL. It should be noted that the prices of crude oil and other feedstocks are not stable and might increase further as well as decrease, for instance due to other (unconventional) oil and gas production methods or improved transport efficiency such as new pipelines. The authors of the 2005 calculation did not include variable feedstock prices in their calculation.

One of the reasons for the unstable oil price are the limited and uncertain worldwide oil reserves. At the moment, in addition to the widely available coal, the world possesses large amounts of natural gas for which the ratio of proved reserves to annual production (R/P) is larger than the R/P of oil [5]. A significant portion of these gas reserves has been assigned 'stranded' because shipping in a gaseous form from the remote location is not economically viable [3]. Furthermore, an equivalent of 30% of the European Union's gas consumption is flared globally as an undesired by-product of oil production [17]. The stranded gas can be directly converted to shippable hydrocarbon liquids by liquefaction to liquid natural gas (LNG), or indirectly by conversion to methanol, ammonia or urea and FTS [1]. The markets and economic incentives for ammonia, urea and methanol are small compared to FT liquids and LNG.

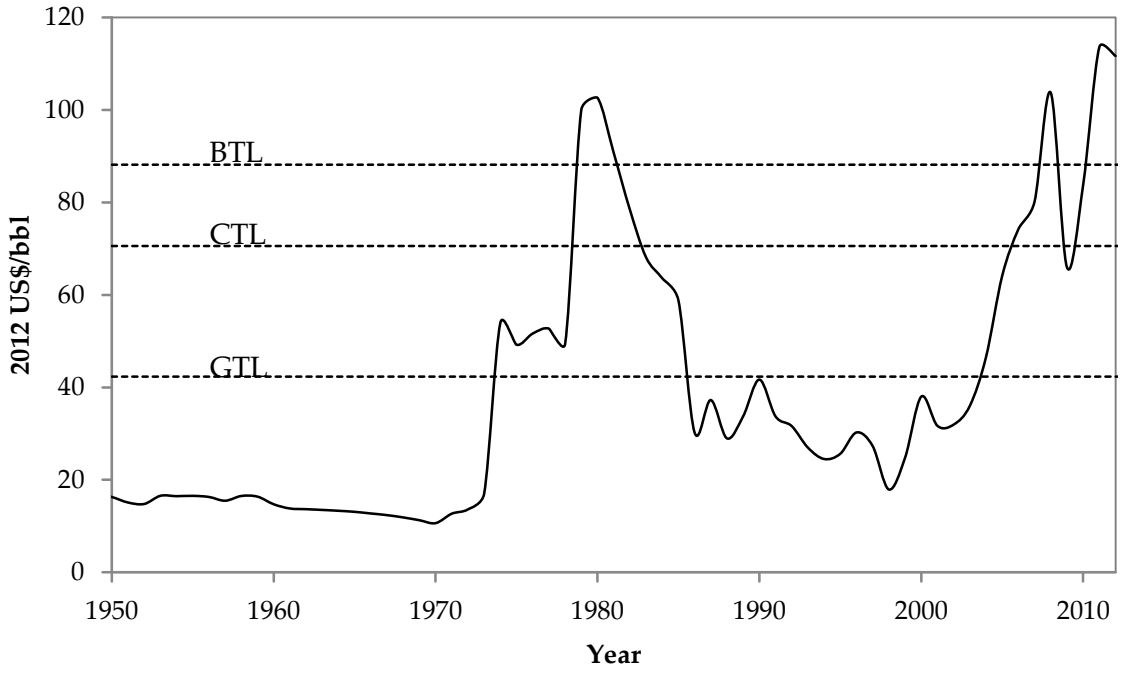

Figure 1.1 Historic crude oil price, inflation corrected (2012) [5]. FTS products become competitive when oil prices rise above US$75/bbl for BTL, $60/bbl for CTL and $36/bbl for GTL [16], assuming the feedstock prices are constant. Due to inflation, these amounts were equivalent to $88.17, $70.54 and $42.32 in 2012, respectively [18]. The horizontal lines show when Fischer-Tropsch alternatives from biomass, coal and natural gas become competitive.

LNG has a thermal efficiency of around 88% (meaning 12% of feedstock energy is needed to produce the final hydrocarbon product) which is high compared to the 60% of GTL. The carbon efficiency of the GTL process is around 77% with the remainder of the carbon from the feedstock being converted to CO_2. LNG production on the other hand has a carbon efficiency of around 88% [19]. Clearly, BTL processes are therefore favored as in that case the CO_2 produced does not originate from fossil feedstocks. However it should be noted that these numbers are limited to production, transportation to the production site and to the consumer are not taken into account.

Emissions resulting from the combustion of fuels (e.g. SO_x, and fine dust) are highly regulated and thus cleaner fuels are required [20]. FT fuels contain fewer impurities than conventionally produced fuels. Sulfur is removed to a large extent in the production of syngas upstream from the FT reactors and the products are free from nitrogen compounds [21] and corrosion causing metal impurities that are present in crude oil (such as Ni, V, Fe, Cu [22]). As a result, SO_x emissions are low when burning FT diesel compared to conventional diesel or biodiesel. Another important property is the high cetane number of FT diesel that is produced from FT products that contain a large concentration of linear alkanes and are free of polycyclic aromatic molecules. Combustion of a fuel without aromatic molecules results in very low soot and fine dust generation [23].

Two large GTL plants have recently been built by SASOL and Shell in Qatar, the latter with a capacity of 260,000 bbl/d [24]. Another 96,000 bbl/d GTL facility is being planned by SASOL in Westlake, Louisiana, USA [25], [26]. Chevron is developing a 33,000 bbl/d GTL facility in Escravos, Nigeria [27]. China is also active: in 2010, a total FT capacity of 7500 bbl/d was operating, with another 600,000 bbl/d CTL capacity being planned [5], [28].

1.2 The Fischer-Tropsch Synthesis

The Fischer-Tropsch process is an exothermic process that converts syngas into hydrocarbons. Alkanes are formed following Equation (1.1) and depending on the catalyst and reaction conditions other reactions can also occur. Alkenes are formed following Equation (1.2) and alcohols following Equation (1.3). The water gas shift reaction (WGS, Equation (1.4)) converts water and carbon monoxide to hydrogen and carbon dioxide and vice versa. The average heat released per 'CH_2' unit is 145 kJ/mol [1], other changes in enthalpy were obtained from heat balance calculations in *Outukumpu HSC Chemistry for Windows 4.1*.

		$\Delta H^0_{298\,\mathrm{K}}$ (kJ/mol)	
alkanes	$(2n+1)\,H_2 + n\,CO \rightarrow C_nH_{(2n+2)} + n\,H_2O$	-206.16 (n=1), -347.26 (n=2)	(1.1)
alkenes	$2n\,H_2 + n\,CO \rightarrow C_nH_{2n} + n\,H_2O$	-210.10 (n=2)	(1.2)
alcohols	$2n\,H_2 + n\,CO \rightarrow C_nH_{2n+1}OH + (n-1)\,H_2O$	-90.63 (n=1)	(1.3)
WGS	$CO + H_2O \leftrightarrows CO_2 + H_2$	-41.14	(1.4)

The catalysts investigated in this work are cobalt FT catalysts. The amount of oxygenates formed on this type of catalysts is very low [29]. Therefore, oxygenates will be neglected.

This section covers the product distribution (Subsection 1.2.1) and the reaction conditions (Subsection 1.2.3). Subsection 1.2.2 gives an introduction to catalysts used in FTS.

1.2.1 Product distribution

The products formed by FTS follow the Anderson-Schulz-Flory (ASF) distribution [1]. The kinetics are schematically drawn in Figure 1.2. A C_nH_x unit bound to the surface of the catalyst has a probability α to grow to a longer chain $C_{n+1}H_y$ and a probability $(1-\alpha)$ to desorb as C_nH_z. The chain growth probability factor α depends on various process parameters such as the catalyst composition and process conditions including syngas composition, temperature and pressure [1].

The weight fraction W_n of hydrocarbon molecules containing n carbon atoms is described by Equation (1.5).

$$W_n/n = (1-\alpha)^2\alpha^{n-1} \tag{1.5}$$

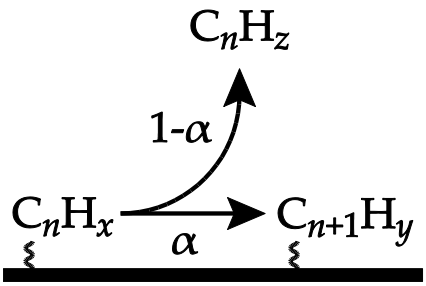

Figure 1.2 Generalized ASF pathway for catalyst surface bound C_nH_x species.

In Figure 1.3, it can be seen that for low values of α the main product is methane and a system with high values of α yields long chain hydrocarbons which are solid at room temperature. For the production of liquid transportation fuels, the waxes are then hydrocracked producing large amounts of high quality diesel [2].

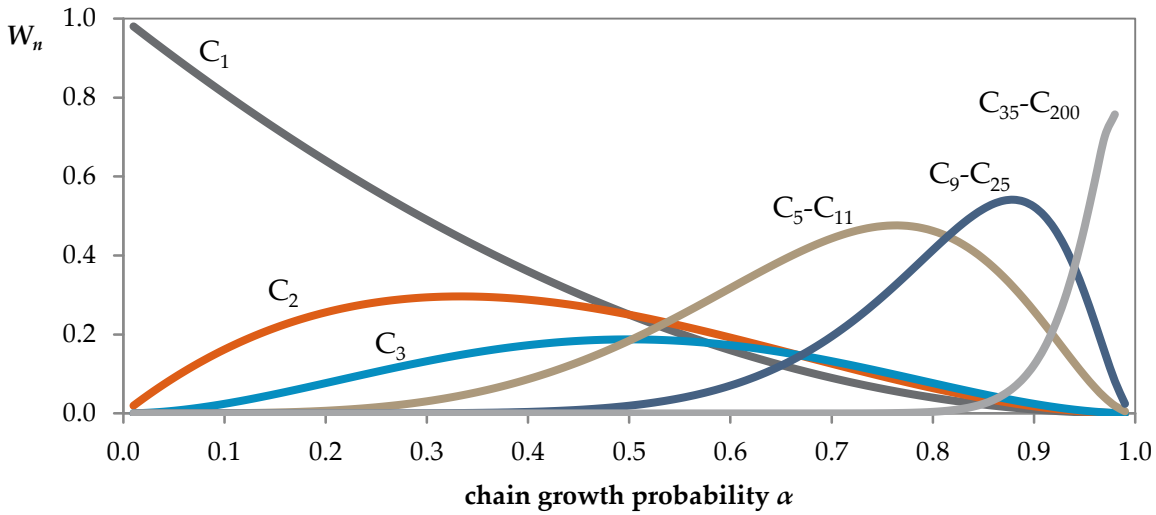

Figure 1.3 Product distribution expected from ASF kinetics.

1.2.2 Catalysts

Catalysts increase the rate of a reaction by lowering the activation energy, without being consumed. As mentioned in the previous subsection, the product distribution depends on the catalyst composition. A successful catalyst has high selectivity towards the desired products, is stable over prolonged periods of time and is highly active. Catalyst design is thus the key to economic viability for industrial processes.

In heterogeneous catalysis, the metals are often supported on metal oxides like SiO_2,TiO_2 or Al_2O_3, some of which are reducible [29]. Using a support enables obtaining metal nanoparticles which have a high surface to volume ratio. As catalytic reactions occur on the metal surface, smaller particles result in a higher catalytic activity per unit mass and volume of the metal. Most support materials have high porosity enabling a high metal surface density and can facilitate heat transfer. Supported metal nanoparticles often have high stability. The metal oxide support might also be chemically active influencing catalytic properties.

Although catalysts are not consumed during the reaction, catalysts do face deactivation. This can be caused by various factors, including poisoning, net particle growth decreasing the specific surface area, carbon effects and fouling and oxidation [30], [31]. This section covers the deactivation factors that are relevant for the FT reaction.

Through poisoning, a compound other than the reactant binds strongly to a catalytically active site, thereby physically blocking the site. Sulfur is such a strong poisonous compound. Depending on the system it might even electronically modify neighboring metal atoms. Due to this electronic modification, one sulfur atom is able to block more than the two active sites blocked geometrically [32]. Other poisoning compounds are less studied and include nitrogen and alkali metals [30]. It is clear that impurities in the syngas are a major concern. Impurities are removed from the syngas feed up to a large extent but even traces can have a significant influence. Therefore, more robust catalysts are desired when the syngas contains sulfur and the catalyst of choice depends on the syngas feedstock. Although sulfur is often undesired, recent research has found that sulfur might also have a promoting effect [33].

Two mechanisms exist for net particle growth, illustrated in Figure 1.4. Due to the increased temperature at which reactions take place, metal atoms and crystallites are more mobile than at room temperature. Coalescence occurs when two clusters touch or collide and merge to form one bigger cluster. In contrast, Ostwald ripening takes place when single atoms are released from one cluster and transferred to another, increasing the size of the latter. This is a dynamic process, but the rate of loss from the smaller cluster is higher because of the lower average coordination of atoms. Therefore, big clusters get bigger and small clusters eventually disappear [34]. Strongly interacting supports like Al_2O_3 retard crystallite diffusion [30].

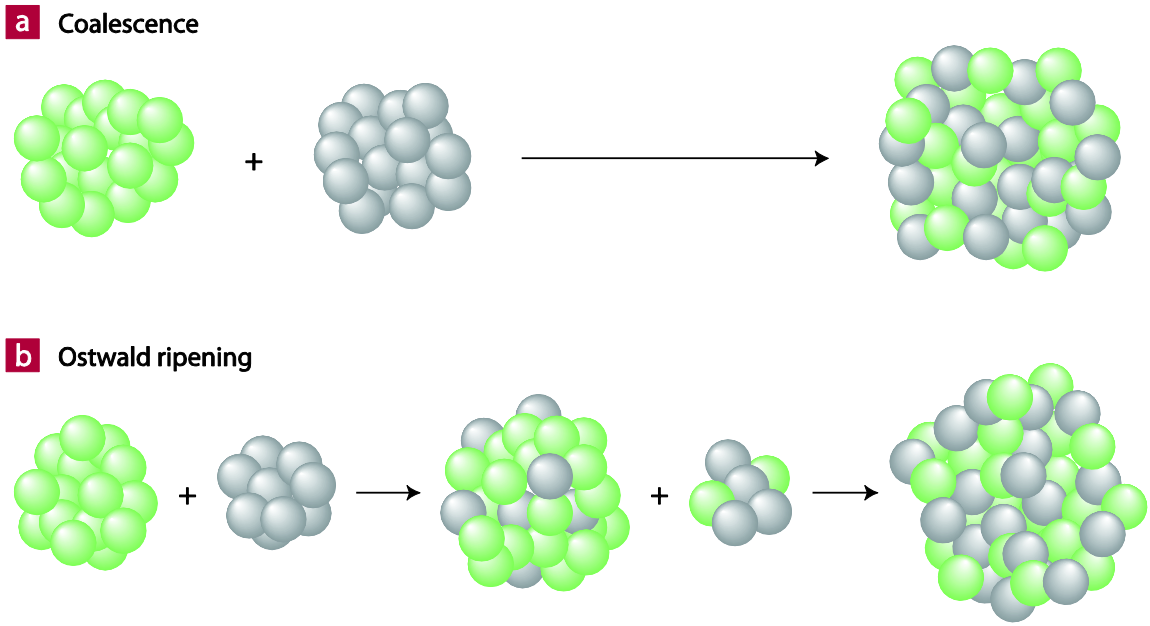

Figure 1.4 Particle growth mechanisms: coalescence and Ostwald ripening (taken from [34]).

The rate at which the particle growth occurs is thus dependent on the support material. The atmosphere is also important: it is known that a high relative humidity induces particle growth [35]. Furthermore, the temperature to which catalysts are exposed also plays a role. Depending on the crystal structure, atoms can already become mobile at the Hüttig temperature which is semi-empirical related to the melting point according to Equation (1.6), and bulk atoms show mobility at the Tamman temperature (Equation (1.7)) [36]. With a melting point at 1768 K [37], cobalt atoms can already become mobile above 257 °C.

$$T_{\text{Hüttig}} = 0.3 \times T_{\text{melting}} \tag{1.6}$$

$$T_{\text{Tamman}} = 0.5 \times T_{\text{melting}} \tag{1.7}$$

In the FT reaction, the dissociation of CO is considered an elementary step. The carbon present on the catalyst is an intermediate species which can be converted to FTS products but the carbon may also be transformed to more stable species over time affecting FTS activity [31].

At present, for the FT reaction in industry, cobalt and iron are the only metals used as FT catalysts. Other FT catalysts are nickel and ruthenium. Nickel shows high methane selectivity at elevated temperature and forms volatile carbonyls at typical FT conditions resulting in loss of metal. Ruthenium is not favored because of its high costs and low availability [1], [3]. In general the choice for iron or cobalt depends on the composition of the syngas used: because of its activity in the WGS reaction, iron is preferred for the conversion of CO rich syngas obtained from the gasification of coal. Furthermore, the robustness of iron catalysts allows conversion of lower-purity syngas such as CTL syngas. For GTL, the feedstock is rich in H_2 and cobalt is preferred [38]. Iron and cobalt have different product selectivity: iron catalysts are able to produce a larger alkene/alkane ratio than cobalt catalysts, cobalt is selective to longer chains and iron also produces oxygenates.

1.2.3 Process conditions

Fischer-Tropsch reactors operate at a temperature either in the range 200–250 °C or in the range 300–350 °C. The first is referred to as low temperature Fischer-Tropsch (LTFT), the latter as high temperature Fischer-Tropsch (HTFT). LTFT and HTFT each have their own reactor types and characteristics [1], [39].

The reactors used in HTFT are fluidized bed reactors: the catalyst (iron) is able to move. The catalyst might circulate (in the circulating fluidized bed reactor) or not circulate (fluidized bed reactor). The operating temperature depends on the product selectivity and a temperature is chosen such to make sure no liquid products are formed. Reactors do not operate above 350 °C as undesired carbon products (including surface carbon species) are formed above this temperature, lowering the catalyst activity. Hence, as the minimum temperature to avoid condensation with a maximum selectivity in the C_{12}–C_{18} range is 468 °C [1], fluid-

ized bed reactors cannot be used for maximized production of products heavier than the gasoline/naphta cut.

Two types of reactors used in LTFT are the tubular fixed bed reactor in which the catalyst (Co or Fe) is not moving and the slurry phase reactor. Due to the relatively low operating temperature, most reaction products, including water, are in the liquid phase.

As the FT reaction is exothermic and catalysts are damaged at high temperature (by particle growth and/or carbon formation), reactors have to be designed in such a way that the heat transfer rate is sufficiently high to maintain near-isothermal conditions.

1.3 Carbon nanotubes as a potential support for Co FTS catalysts

After the discovery of the material in 1991 [40], carbon nanotubes (CNT) have quickly gained interest. Numerous potential applications have already been demonstrated [41]. Two main types of CNT exist: single-walled CNT (SWCNT) and multi-walled CNT (MWCNT). Both types are drawn schematically in Figure 1.5.

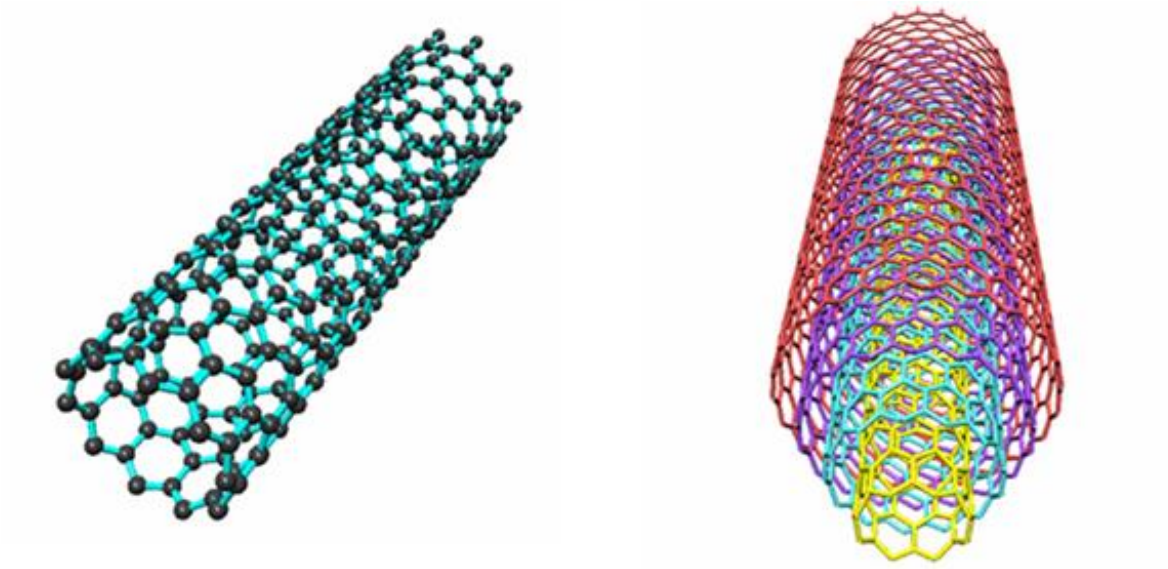

Figure 1.5 Single-walled CNT (left) and multi-walled CNT [41].

CNT are rolled-up graphene sheets: SWCNT are composed of a single sheet whereas MWCNT are composed of multiple sheets, arranged in a Russian nested doll fashion. A method for large scale production of MWCNT is chemical vapor deposition, in which 1 g of spinel-type cobalt–manganese-based mixed oxide catalyst can produce about 180 g of MWCNT, when exposed to an ethylene/hydrogen feed at 650 °C for 2 h [42].

CNT are inert and have a high chemical stability in aggressive media. The material has a well-defined structure and high mechanical strength and is thermally highly stable. Precious

metals supported on CNT can be recovered by burning the support [43]. This makes the CNT an interesting support material in catalysis.

Due to the inertness, CNT are not able to interact strongly with metals that are supported. Nevertheless, it is possible to modify the surface in order to introduce anchoring sites for metals. When using carbon materials as a support in catalysis, the material is often pre-treated with an oxidizing agent like concentrated nitric acid, removing impurities and introducing oxygen containing groups as anchoring sites [44]. The metal is often loaded on the support by impregnation with an aqueous metal precursor solution or by deposition precipitation [45], [46].

The cost of CNT as a support material is currently high compared to other support materials. According to Su *et al.*, industrial application of CNT in catalysis is therefore limited to the clean and sustainable energy sector, although new opportunities are emerging in the chemical synthesis area [47].

1.4 Scope of this thesis

The oxidative treatment applied to carbon nanotubes not only removes metal impurities from the carbon nanotubes but also changes the smooth and inert carbon surface into a rough surface on which oxygen groups are present. These oxygen groups are thought to be necessary as anchoring sites for the catalyst metal and change the affinity to different solvents: plain CNT are apolar whereas oxygen groups on the surface introduce polar sites.

In this work, the influence of the surface treatment and the choice of the impregnation solvent were investigated by comparing catalytic activity, selectivity and stability of different catalysts. The CNT surface treatments that were investigated are illustrated in Figure 1.6 which shows the as-received CNT, the rough, oxidized CNT with oxygen groups on the surface and the rough reduced oxidized CNT without oxygen groups on the surface.

In Chapter 2, the support material will be described. The untreated support will be analyzed along with treated support samples. Continuing with these supports, Chapter 3 covers the further synthesis, characterization and performance tests of the prepared catalysts. The catalytic performance of the catalysts is tested in Chapter 4, before the results are summarized and an outlook is given in Chapter 5.

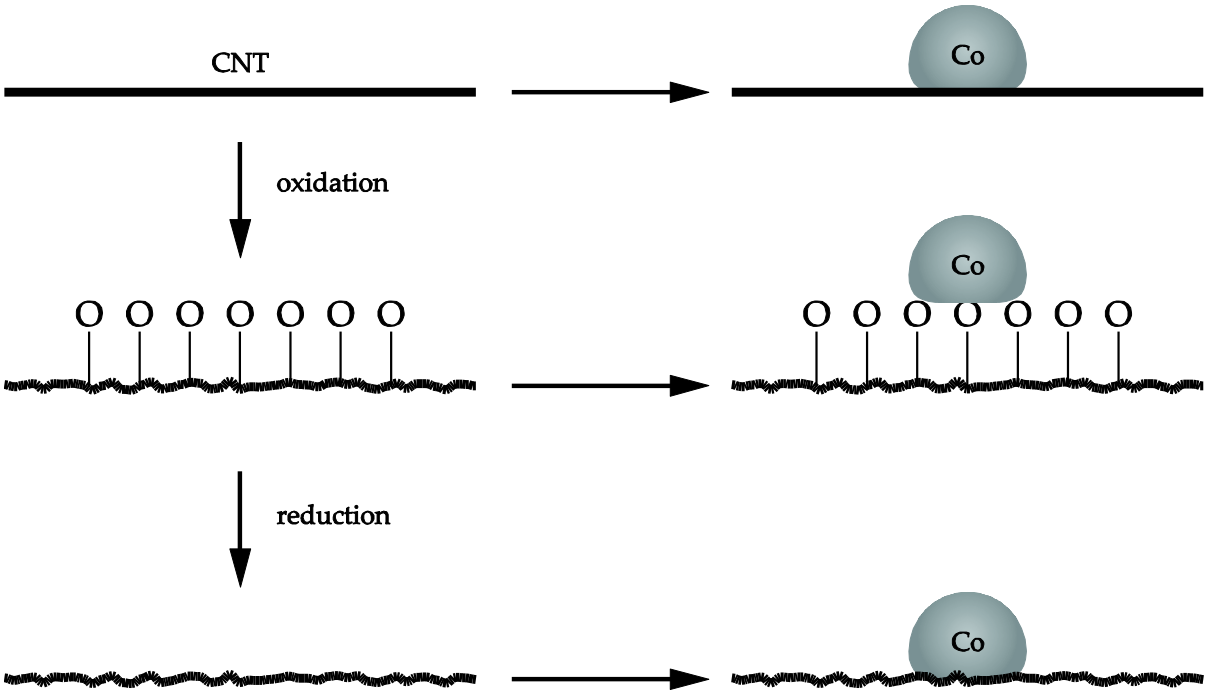

Figure 1.6 Preparation pathways

Chapter 2

Support preparation and characterization

2.1 Introduction

In this project, multi-walled carbon nanotubes (MWCNT) were used as support material. The MWCNT were manufactured by Bayer as Baytubes C 150 HP. The as-received material has high purity and a total carbon content above 99%. The Baytubes C 150 HP were designated as CNT.

Although the Baytubes have high purity, traces of the growth catalyst may be contained. Metal impurities are Mg, Al, Mn and Co. Mn is known for having promoting effects in the FT reaction [46]. However, for promoting effects, the Mn has to be in close vicinity to the actual catalytically active metal. As a growth catalyst for carbon nanotubes, the metal is entrapped within the carbon nanotubes. Possible impurities not inside the CNT have been removed in the additional purification step performed by Bayer. When using CNT as a catalyst support, the catalytically active metal is located on the outside of the tubes. Therefore, the possible presence of manganese is not likely to influence catalytic properties. Nevertheless, effects on catalytic performance will be checked in Chapter 4.

Common surface treatments applied to CNT are liquid phase oxidation (LPO) and gas phase oxidation (GPO). The most common treatment is liquid phase oxidation by a strong acid like nitric acid, a mixture of strong acids like nitric acid and sulfuric acid and in some cases diluted nitric acid [49]. This introduces oxygen groups (Figure 2.1 shows the oxygen groups that can be introduced this way) and has shown to increase the binding strength between metal and CNT surface for copper [50] which might also be the case for cobalt. The oxygen groups can be further modified or used to introduce other functional groups [51].

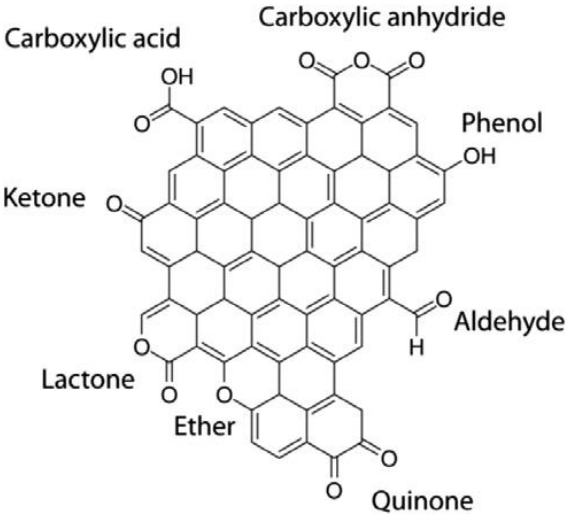

Figure 2.1 Oxygen containing groups introduced by oxidation of the CNT surface [48]

LPO treatment is not limited to introducing functional groups, but also damages the CNT surface. Furthermore, LPO requires extensive

purification (filtering, washing and drying) after the treatment. As an alternative, GPO has shown to be a highly efficient route for introducing oxygen groups on the surface of carbon nanotubes [52]. As a relatively mild treatment, these groups are mainly carboxyl groups and the structural damage is limited. The structural damage of LPO and GPO is compared in Figure 2.2.

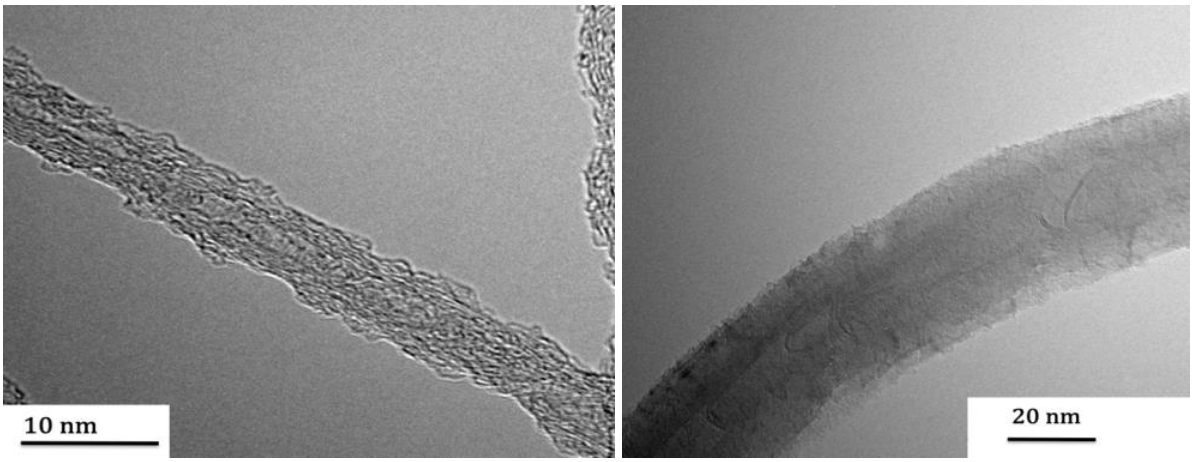

Figure 2.2 TEM pictures of multi-walled CNT treated by LPO (left) and GPO (right) [53].

In this research, the CNT surface treatment was GPO. To study the effects of the structural defects but without the presence of oxygen containing groups, the oxygen containing groups in the GPO-treated samples will also be removed. Carbon nanotubes are a graphene-like material. As graphene oxide is expected to be reducible by hydrogen [54], oxidized carbon nanotubes are likely to be reducible by hydrogen as well. By first applying an oxidative treatment and subsequently reducing the system, the structural damage to the CNT is thought to remain intact while the oxygen containing groups are removed.

In this chapter, Section 2.2 describes the experimental procedure. The properties of the GPO-treated CNT are analyzed and compared with untreated CNT in Section 2.3.

2.2 Experimental

2.2.1 Oxidation

Gas phase oxidation was carried out using the setup shown in Figure 2.3 [48], [52]. The design of the setup prevents the reflux of liquid from the condenser to the sample: the liquid nitric acid flows back to the round bottom flask below the sample holder. A 0.4 g sample of untreated CNT was dried for 2 hours at 125 °C (which is above the boiling point of nitric acid (120 °C [55])) inside the reactor oven. Then, the Allihn condenser and round bottom flask containing about 150 mL HNO_3 (65%) were connected to the oven and the nitric acid was heated quickly using a heating mantle. The nitric acid was kept boiling for 0.5–4 h. Then the heating mantle was removed and the nitric acid was allowed to cool and condensate for

1 h after which the setup was dismantled, keeping the oven with the oxidized sample at 125 °C for another 1 h. To make sure samples were free of nitric acid some samples were transferred to a static oven and kept at 120 °C in air for 16 h.

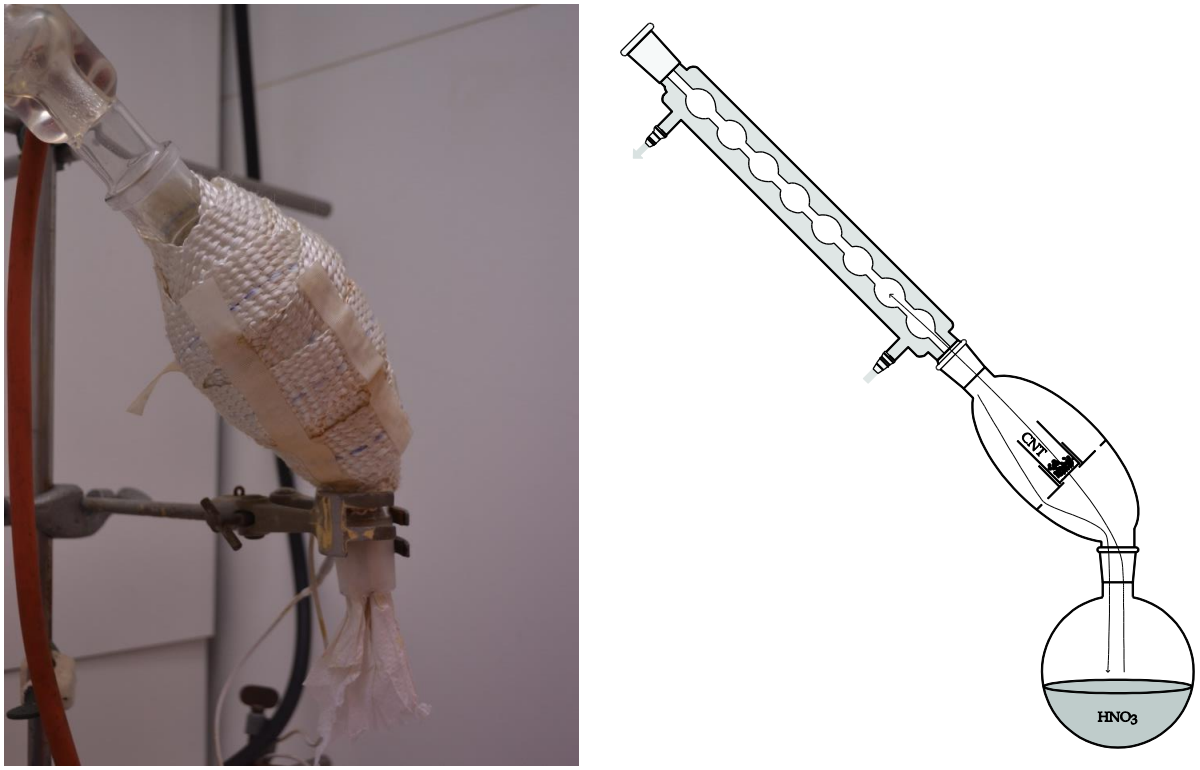

Figure 2.3 Setup used for gas phase oxidation: actual setup without HNO_3 flask (left) and schematic drawing including the HNO_3 flask (right). The setup was completed with a heating mantle around the HNO_3 flask and an exhaust line. The sample oven is fitted with a trace heating mantle.

2.2.2 Reduction

For the removal of the acid groups by hydrogen, a sample of about 0.5 g was loaded in a glass tubular reactor. In a pure hydrogen flow of 250 mL/min (fixed bed), the sample was heated to the temperature found from the TPR experiment (i.e. 550 °C (Section 2.3.1)) at a temperature ramp of 10 °C/min. The sample was kept at this temperature for 1 h. After switching off the heating, the gas flow was changed to nitrogen.

2.2.3 Characterization

Temperature programmed reduction

The temperature needed for the removal of the acid groups by hydrogen was investigated by a temperature programmed reduction (TPR) experiment. This was performed on GPO treated CNT using a Micromeritics AutoChem II 2920. The sample was dried for 15 min at 120 °C (ramp rate 10 °C/min) under a flow of argon. The gas flow was switched to 5% H_2 in Ar (50.10 cm^3 STP/min) and the temperature was increased to 800 °C (ramp rate 10 °C/min).

Titrations

To obtain information on the amount of acid groups introduced by oxidation, titrations were performed using a Radiometer Analytical TitraLab TIM880 titration manager. Typically, 25–50 mg of the sample was loaded and 60 mL 0.1 M KCl (aq) was added, while stirring. In order to remove dissolved CO_2, nitrogen was bubbled through the liquid for two minutes before adding the titrant. The sample was titrated using an aqueous solution containing 0.01 M NaOH and 0.1 M KCl until the pH reached 9 or until the added volume of the titrant was 5 mL.

The inflection point in the pH curves can be found by calculating the second derivative and finding v for which the equation $\frac{d^2pH}{dv^2} = 0$ holds. However, this method is very sensitive to slight deviations from ideal behavior. Therefore, as an alternative route, the inflection point was found by numerically calculating the first derivative (which has a maximum at the inflection point) and then applying a second degree polynomial fit ($y = av^2 + bv + c$) around the maximum, finding the inflection point by calculating $v_{\text{inflection}} = -b/2a$.

TEM

TEM images were obtained using Philips Tecnai 12 and Philips Tecnai 20 transmission electron microscopes. Samples were prepared by ultrasonic dispersion of a grinded sample in ethanol and then applying a few drops on a holey carbon copper grid.

XRD

The support samples were also analyzed by x-ray diffraction (XRD) on a Bruker D2 Phaser x-ray powder diffractometer using CoK_α radiation. Patterns were recorded in the range 2θ=10°–80°.

TGA

CNT are known for the high thermal stability, as mentioned in the introduction. To find the influence of a GPO treatment on the thermal stability of CNT, a thermogravimetric analysis (TGA) was performed. Using a PerkinElmer Pyris 1 TGA, a 1 mg sample was heated from 50 °C to 700 °C at a ramp rate of 5 °C/min in a nitrogen flow of 20 mL/min, continuously recording the sample mass.

2.3 Characterization

2.3.1 Reducibility

Results from the TPR experiment are shown in Figure 2.4. The maximum hydrogen uptake was found near a temperature of 550 °C. At this temperature, the acid groups are expected to be removed.

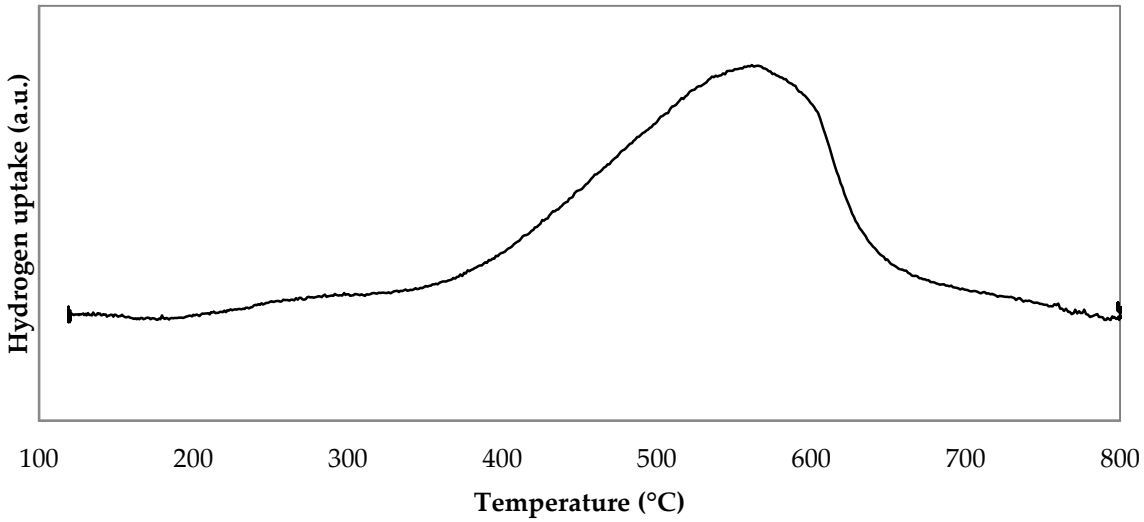

Figure 2.4 TPR data for a 2 h gas phase oxidized CNT sample.

2.3.2 Acid group content

A typical pH curve obtained by titrations is shown in Figure 2.5.

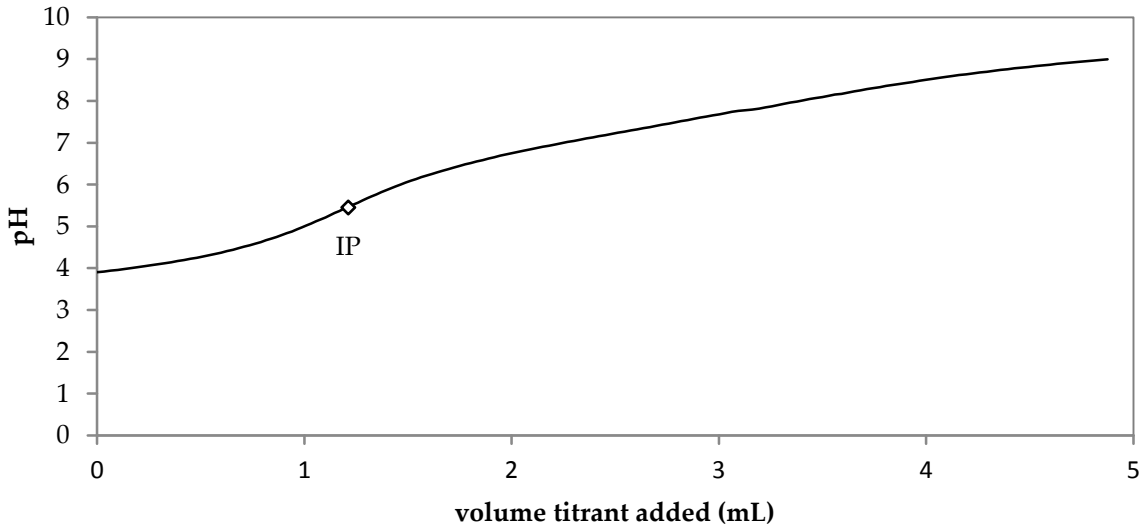

Figure 2.5 Typical pH curve for a sample that has been acid treated for 2 hours. The inflection point (IP) was found at v=1.21 mL.

The amount of acid groups in the samples is shown in Figure 2.6.

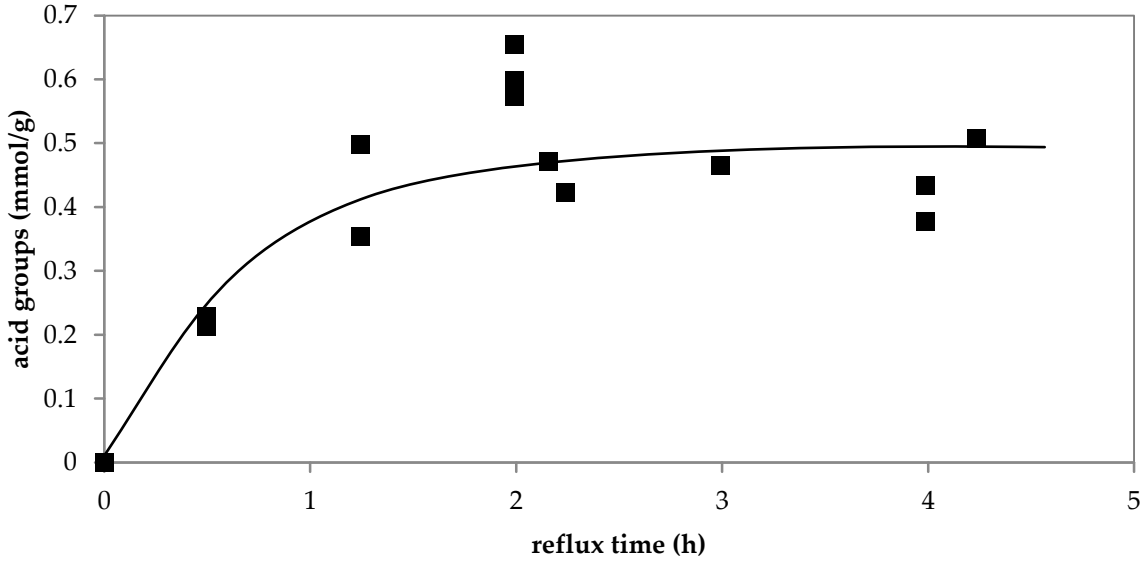

Figure 2.6 Amount of acid groups on the CNT surface, determined numerically by finding the inflection point of the pH curve obtained by titration. The line through the points is drawn as a guide to the eye.

It is seen that the acid group content introduced by GPO increases in the first two hours and then becomes constant. The rapid increase in the first hours is in accordance with earlier research [52], and the amount of acid groups is in the same order of magnitude as carbon nanofibers that have been treated similarly [48]. However, it can also be seen that the content of acid groups introduced by GPO treatment is either hard to control or hard to measure using titration. In an attempt to increase the reproducibility, an additional drying step of 16 h at 120 °C in static air before the titration was introduced. This was done to make sure no nitric acid was present in the sample but did not significantly improve the consistency and reproducibility.

Another reason for the bad reproducibility of the titration might be found in the GPO treatment procedure itself. After the desired oxidation time was reached, the heating mantle was removed but for safety, the setup was not disassembled immediately but after an hour. During this hour, nitric acid vapor was still present, though in a lower concentration. This might have introduced an error in the oxidation time resulting in a less reliable acid groups to oxidation time ratio.

Titration experiments on samples that were reduced by hydrogen after the GPO treatment showed no acid group content. Therefore, the reduction method appeared to be successful.

2.3.3 Morphology

It is seen in TEM images (Figure 2.7) that GPO treatment introduces minor structural defects. The dark patches seen in the CNT walls are assigned to be diffraction contrast.

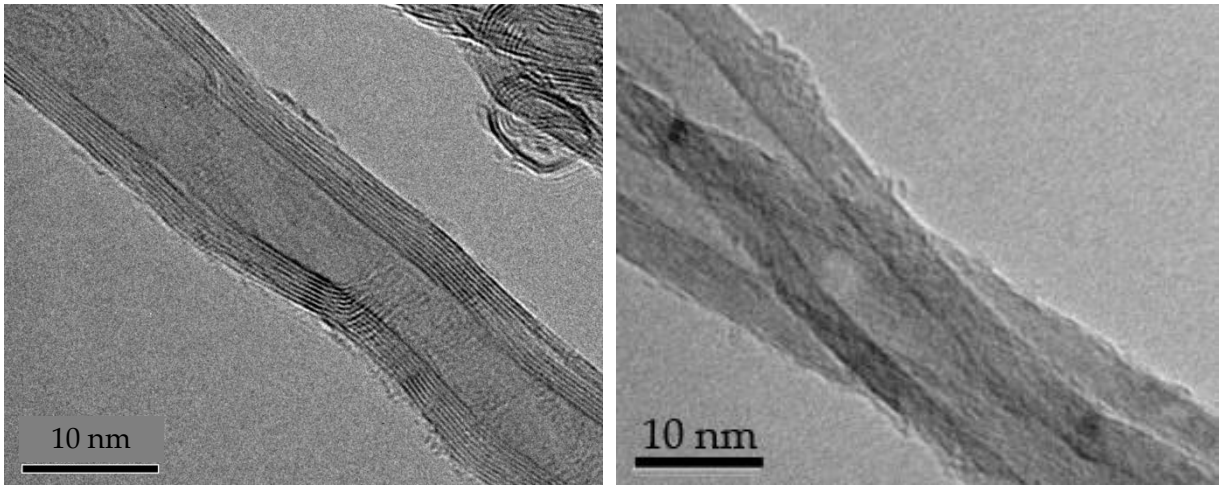

Figure 2.7 TEM images of untreated CNT (left) and a gas phase oxidized CNT sample [56].

Typical XRD patterns are shown in Figure 3.10 (Chapter 3, page 33). It is seen that oxidation does not significantly influence the XRD patterns: untreated CNT and 0.5 h GPO CNT show the same signals. From this it is concluded that the GPO treatment does not distort the crystallinity of the CNT.

As expected, from both TEM and XRD it is seen that the overall morphology of the CNT is still intact although minor damage to the surface is recognized in TEM images. Earlier nitrogen physisorption experiments confirm that gas phase oxidation has a small influence on porosity and surface area compared to liquid phase oxidation (Table 2.1).

Table 2.1 Influence of the oxidation treatments on specific surface areas (taken from [56]).

Support	B.E.T. area (10^2 m^2/g)	Micropore area (m^2/g)	Total pore volume (mL/g)
CNT	2.0	24	1.2
2.5 h GPO CNT	2.5	18	1.4
0.5 h LPO CNT	2.4	16	1.4
2 h LPO CNT	2.7	14	1.1

2.3.4 Thermal stability

The results of the thermogravimetric analysis are plotted in Figure 2.8 alongside with an earlier experiment on untreated CNT. From the TGA plot, it is seen that applying a GPO treatment on CNT reduces the thermal stability, although the total weight loss by heating to 700 °C in an inert atmosphere remains below 10%, and more relevant: the weight loss for the oxidized sample is only 2% up to a temperature of 350 °C

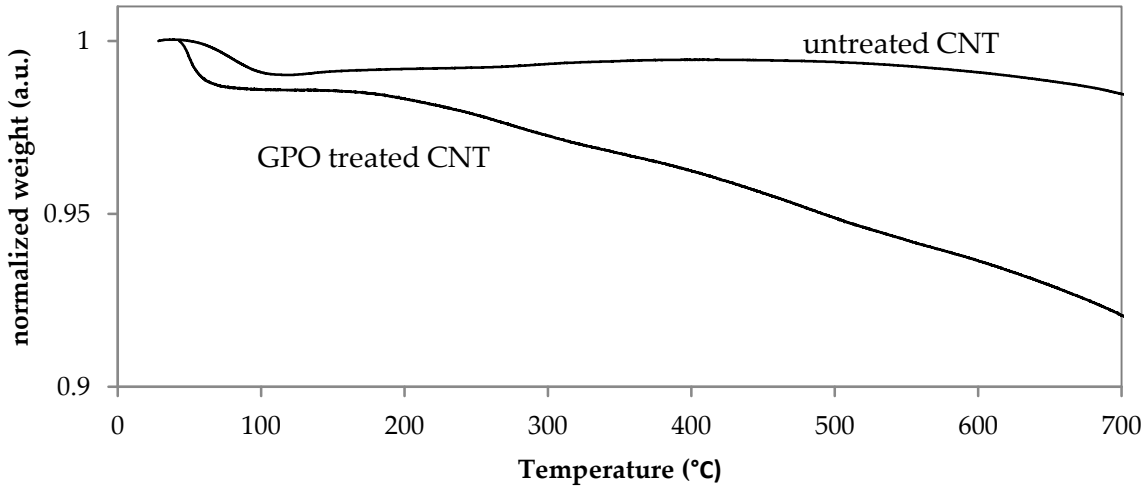

Figure 2.8 TGA data for untreated CNT (top, data taken from René Manchester) and 4.25 h GPO CNT (bottom). Untreated CNT are more stable than oxidized CNT. The weight loss below 100 °C is ascribed to loss of water.

2.4 Summary and outlook

CNT were treated by nitric acid vapor, introducing acid groups. The amount of acid groups was related to the treatment time: by titrations, an increase in acid group content was seen in the first two hours of treatment time, and the amount of acid groups stabilized at about 0.45 mmol/g after 2 hours of treating. The reproducibility of the determination of the acid group content by titrations was difficult: GPO is either hard to control or the titration method is not the best way for measuring the amount of acid groups.

In a temperature programmed reduction experiment, the GPO treated samples showed a hydrogen uptake with a maximum at a temperature near 550 °C. This uptake was attributed to the removal of surface oxygen species. Titration experiments confirmed the absence of acid groups on samples that were reduced in flowing hydrogen at 550 °C after the GPO treatment.

The overall structure of the GPO treated CNT was shown to remain intact by TEM imaging, x-ray diffraction and earlier nitrogen physisorption experiments. Only minor damages were seen in TEM and the porosity and surface area changed slightly, but the crystallinity of the CNT was not distorted severely.

To verify the amount of acid groups introduced by GPO, other techniques are necessary. X-ray photoelectron spectroscopy (XPS) can be used to identify the nature and concentration of oxygen containing groups near the surface [52], whereas an elemental analysis can determine the full oxygen content but not its nature, which can in turn be investigated by infrared spectroscopy. The defect density can be determined by performing Raman spectroscopy and calculating the ratio between the D-band and the G-band [57].

Chapter 3

Catalyst preparation and characterization

Using the as-received CNT and CNT with different pre-treatments, different catalysts were synthesized. The theoretical background of these syntheses is described in Section 3.1. Section 3.2 describes the experimental procedure. The catalysts were characterized by x-ray diffraction, transmission electron microscopy, temperature programmed reduction, thermogravimetric analysis and hydrogen chemisorption (Section 3.3).

3.1 Theory

The catalysts were prepared by incipient wetness impregnation of the support material, followed by a drying step and thermal treatment. The impregnation solvents that were investigated are water, ethanol and 1-propanol.

3.1.1 Incipient wetness impregnation

The metal was loaded on the support by incipient wetness impregnation. This method is carried out by contacting a previously dried support with a precursor solution of which the volume is equal to the support sample's pore volume. In the case of proper wetting and previously empty support particles, the solution is fully drawn into the pores [58]. In order to remove water from the pores of the support particles, the support needs to be dried at elevated temperature and reduced pressure prior to impregnation. The reduced pressure needs to be maintained during the impregnation to make sure that condensation of atmospheric water vapor has no influence.

There are several important factors in the choice of a suitable solvent for incipient wetness impregnation. Beside e.g. the environmental impact, disposability and recycling options, three factors will be treated here. The wetting capability on the support material needs to be sufficiently high, the metal precursor needs to be soluble up to the desired concentration and to avoid cooling steps it is convenient in lab scale experiments to choose a solvent that has a sufficiently high boiling point.

The solvent used for the precursor solution needs to be able to wet the surface of the support material, in other words, the wetting capabilities of the solvent need to be sufficient. In capillary impregnation, the driving force is the capillary pressure P_{cap} which depends on solution

surface tension σ_L, wetting angle θ (Figure 3.1) and characteristic pore size r, according to Equation (3.1) [59].

$$P_{cap} = \frac{2\sigma_L \cos\theta}{r} \tag{3.1}$$

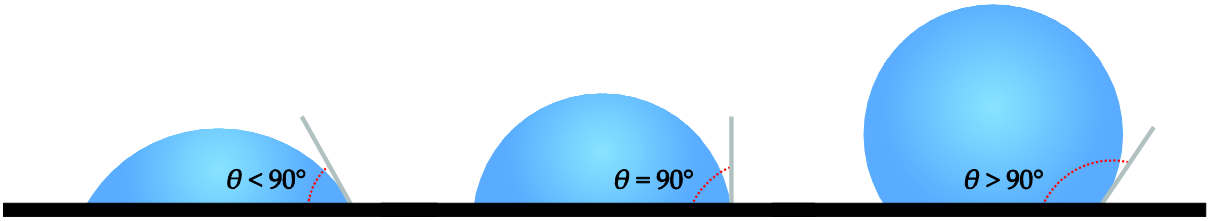

Figure 3.1 Wetting angle θ illustrated in drops of a liquid on a surface.

It is recognized that in order to have a high surface wetting with limited amounts of liquids such as in the drying process following incipient wetness impregnation, the wetting angle θ needs to be smaller than 90°. When a good solvent is used, the capillary pressure draws the solution into the pores of the catalyst particles and the surface wetting is high whereas when a bad solvent is used, the surface wetting is low. When the pores of the CNT agglomerates is completely filled, the density of CNT will be comparable to the density of graphite (2.2 g cm^{-3} [37]), while when the pores remain (almost) empty the density of the CNT will be significantly lower, close to the bulk density of the CNT particles (0.12–0.17 g cm^{-3} [60]) caused by entrapped air. As common solvents have a density between 0.6 and 1.6 g cm^{-3} (including water, ethanol and 1-propanol [37]), which is lower than the graphite density, a simple test can show whether the solvent has good or bad wetting properties. After sprinkling some CNT agglomerates on a sample of a solvent, the particles can either float (density of the agglomerates is lower than the density of the solvent or the pores remain empty so the solvent does not have good wetting capabilities) or sink (density of the agglormerates is higher than the density of the solvent and the pores are filled so the solvent has good wetting capabilities).

It has been shown before that impregnating CNT with a solution of cobalt nitrate hexahydrate in ethanol leads to a better dispersion of the metal particles after drying and thermal treatment [56].

The second important parameter is the solubility of the metal precursor. This needs to be high enough to obtain the desired metal loading on the catalyst. In the case of cobalt, the metal loading is defined as the mass of cobalt divided by the mass of the support material plus the mass of cobalt oxide, assuming the cobalt is fully oxidized as Co_3O_4. For a metal loading of about 10% on the CNT achieved in a single step impregnation it is necessary to use a precursor solution with a concentration of 1.5 M: impregnation of 1 g CNT with 1.2 mL of 1.5 M Co precursor solution yields a 9% weight loading. The highly soluble cobalt nitrate hexahydrate ($Co(NO_3)_2 \cdot 6\,H_2O$) is chosen as the metal precursor. Besides the high solubility,

this compound is readily available and well affordable. The compound easily thermally decomposes to yield cobalt oxide.

The last important parameter treated is the boiling point of the solvent. As the impregnations are carried out in vacuum, the solvent might evaporate immediately at this reduced pressure. It is known that when using ethanol as impregnation solvent, both the setup and the impregnation solution has to be cooled down before impregnation [56], [61].

3.1.2 Drying and thermal treatment

After the impregnation, the solvent needs to be removed. Earlier research has shown that the optimal drying atmosphere is a flow of nitrogen at elevated temperature [56], but cautiousness should be taken in order to keep the precursor intact as other species are already formed slightly above 100 °C [62]. After drying, the precursor needs to be decomposed. This is done by a thermal treatment which will be carried out immediately after drying, by a further temperature increase up to 250 °C. The precursor will decompose into Co_3O_4 [62].

3.1.3 Reduction

CNT supported cobalt oxide has shown to be reducible at 350 °C in flowing hydrogen [56]. The mechanism of the reduction of cobalt(II,III)oxide by hydrogen is a two-step process [63]:

$$Co_3O_4 + H_2 \rightarrow 3\ CoO + H_2O \tag{3.2}$$

$$3\ CoO + 3\ H_2 \rightarrow 3\ Co + 3\ H_2O \tag{3.3}$$

The amount of hydrogen necessary for the two-step formation of 1 mol metallic cobalt is ⅓ mol in the first step and 1 mol in the second step in respect to the amount of cobalt.

3.2 Experimental

3.2.1 Catalyst synthesis

A 0.3–1 g support sample was dried for at least 1 hour in vacuum at 100–150 °C. While maintaining the reduced pressure from the drying step, the heating mantle was removed, allowing the support to cool down to room temperature or lower by cooling on ice if the impregnation solvent used was ethanol. The support was impregnated by adding the amount of precursor solution equal to the pore volume of the support, which is 1.2 mL/g. For ethanol impregnations, the syringe containing the precursor solution was cooled on ice prior to impregnation. The impregnation was done drop-wise from a syringe, mixing by gently shaking. Atmospheric pressure was re-applied and the impregnated support was transferred to a glass tubular reactor. The impregnated samples were then dried and thermally treated to form small Co_3O_4 particles on the support. Samples were dried in flowing N_2 (250 mL/min, 1 atm) at 80 °C (60 °C for ethanol impregnations), fluidized or fixed bed, for

4 hours and subsequently the sample was thermally treated at 250 °C for 4 hours with a ramp rate of 2 °C/min [56]. The mass loading is determined by applying Equation (3.4).

$$\text{Co loading (wt\%)} = \frac{m_{\text{Co}}}{m_{\text{support}} + m_{\text{Co}_3\text{O}_4}} \times 100\% \tag{3.4}$$

Catalyst naming

Systematic names were assigned to the prepared catalysts. All catalysts were prepared by incipient wetness impregnation of carbon nanotubes using cobalt nitrate hexahydrate as the precursor, obtaining a Co loading of about 10 wt%. Only the variable conditions are included in the naming system. The scheme below shows the naming system:

Support	Impregnation solvent	Batch number
CNT	PrOH	1
CNT: untreated CNT **#hGPO:** GPO treated CNT, oxidation time # h **R#hGPO:** reduced GPO treated CNT, oxidation time # h	**PrOH:** 1-propanol **EtOH:** ethanol **H2O:** water	

Catalyst R0.5hGPO-PrOH-1 is obtained by impregnating a CNT sample that has been gas phase oxidized for 0.5 h and subsequently reduced by hydrogen gas at 550 °C. The impregnation solvent was 1-propanol and it is the first batch prepared this way.

3.2.2 Catalyst characterization

Transmission electron microscopy (TEM) images were recorded in normal scanning bright field mode, in high angle annular dark field mode and using a secondary electron detector. The samples were prepared using the method from subsection 2.2.3. Using images obtained by TEM, the morphology and the Co_3O_4 particle sizes were determined by measuring the size of Co_3O_4 particles and averaging these values.

X-ray diffraction patterns were obtained on a Bruker D2 Phaser using CoK_α radiation, measuring in the 2θ range 10°–80°. The step size was 0.15°. No baseline correction was performed. Co_3O_4 crystallite size estimation was performed using the 2θ range from 34°–47° by an automatic calculation in DiffracEvaluation V2.0 software by Bruker, which is based on the Debye–Scherrer-equation [64].

The equivalent metallic Co particle sizes were calculated by applying a molar volume correction factor on the average Co_3O_4 particle size determined by XRD and TEM [65]:

$$d_{\text{Co}} = 0.75 \times d_{\text{Co304}} \tag{3.5}$$

3.2.3 Hydrogen chemisorption

Hydrogen chemisorption was analyzed on a Micromeritics ASAP 2020C. Samples were dried in flowing helium at 100 °C for 1 h. Then, the samples were reduced for 2 h at 350 °C (ramp rate 5 °C/min) in flowing H_2. Subsequently, the samples were evacuated and analyzed at 150 °C using H_2.

Metallic cobalt (Co^0) particle sizes were estimated from the total amount of both reversible and irreversible amount of chemisorbed H_2 by extrapolating the linear plot of the first analysis, assuming complete reduction, a H/Co atomic ratio stoichiometry of 1 and a hemispherical particle size geometry as described by Reuel and Bartholomew [66].

3.2.4 Temperature programmed reduction

Temperature programmed reduction measurements were performed on a Micromeritics AutoChem II 2920. The samples were dried for 15 min at 70 °C (ramp rate 10 °C/min) under a flow of argon. The gas flow was switched to 5 vol% H_2 in Ar (50.17 cm^3 STP/min) and after 32 minutes the temperature was increased to 600 °C (ramp rate 2 °C/min). The hydrogen consumption was determined by a TCD.

3.2.5 Thermogravimetric analysis

Thermogravimetric analyses were performed on a PerkinElmer Pyris 1 TGA. For this, a 1 mg sample was heated from 50 °C to 700 °C at a ramp rate of 5 °C/min in a nitrogen flow of 20 mL/min, continuously recording the sample mass.

3.3 Results and Characterization

The catalysts that have been prepared are listed with their relevant properties in Table 3.1.

In this work, comparisons will be made to catalyst sample INE8. This catalyst is prepared by René Manchester and contains 8% Co on untreated CNT, impregnated with a solution of cobalt nitrate hexahydrate in ethanol [56].

This section will describe the catalysts that have been prepared.

Table 3.1 Prepared Co/CNT catalysts. Catalysts were dried and thermally treated in a fixed bed reactor unless otherwise indicated.

				Co particle size (nm)		
Catalyst	GPO time (h)	Solvent	Co loading	XRD	H_2	TEM (*n*)
CNT-PrOH-1[p,f]	-	1-propanol	9%	2.4		
CNT-PrOH-2[h,f]	-	1-propanol	9%	2.7	5.3	
CNT-PrOH-3	-	1-propanol	10%	3.0		
CNT-PrOH-4	-	1-propanol	10%	n.d.		
CNT-EtOH-5	-	ethanol	10%	3.1		
CNT-EtOH-6	-	ethanol	9%	3.3		3.8 (53)
CNT-H2O-1	-	water	9%	4.2		
0.5hGPO-PrOH-1[f]	0.5	1-propanol	10%	3.2		
0.5hGPO-PrOH-2[f]	0.5	1-propanol	9%	2.9	6.7	
1.25hGPO-PrOH-1	1.25	1-propanol	10%	3.2		
1.25hGPO-PrOH-2	1.25	1-propanol	10%	2.8		
2hGPO-PrOH-1[f]	2	1-propanol	9%	3.7		
2hGPO-PrOH-2	2	1-propanol	10%	2.5		3.3 (31)
4hGPO-PrOH-1	4	1-propanol	9%	3.3		
R0.5hGPO-PrOH-1[f]	0.5[r]	1-propanol	10%	3.8		
R2hGPO-PrOH-1	2[r]	1-propanol	10%	3.3		
2hGPO-EtOH-1	2	ethanol	10%	3.4		3.9 (11)
2hGPO-H2O-1	2	water	10%	3.8		4.3 (8)

[f] catalyst was dried and thermally treated in a fluidized bed reactor

[h] higher N_2 flow during drying and thermal treatment: 1000 mL/min

[p] catalyst was reduced and passivated after thermal treatment

[r] additional surface treatment after GPO, 550 °C in a flow of H_2.

3.3.1 Solvent properties

The wetting capabilities of water, ethanol and 1-propanol were investigated by sprinkling an untreated CNT sample on each solvent. Figure 3.2 shows that water has bad wetting capabilities while ethanol and 1-propanol have good wetting capabilities.

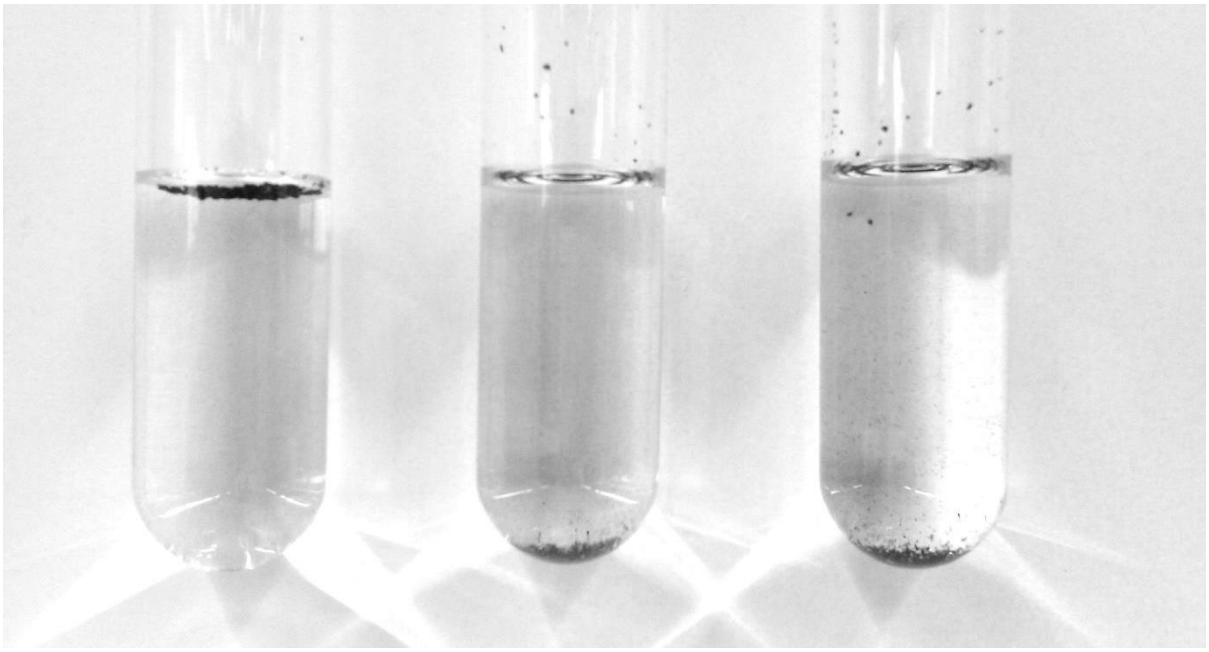

Figure 3.2 Behavior of untreated carbon nanotubes sprinkled on different solvents. CNT float on water (left) but sink in ethanol (middle) and 1-propanol (right).

1-propanol combines the advantages of water (high boiling point) and ethanol (proper wetting) and although the solubility of cobalt nitrate is low, it is still high enough to prepare a 1.5 M solution. Therefore, most catalysts in this research will be prepared by using 1-propanol as the impregnation solvent. Water and ethanol will also be treated.

Table 3.2 summarizes the relevant solvent properties of water, ethanol and propanol.

Table 3.2 Relevant solvent properties of water, ethanol and propanol for IWI on CNT. The solubility was determined experimentally and is not necessarily the maximum solubility.

	CNT wetting	boiling point (°C) [55] 1 atm	50 mbar	cobalt nitrate solubility (M)
water	bad	100	33	4
ethanol	good	78	17	2
1-propanol	good	97	34	1.5

3.3.2 Morphology

TEM images were recorded and the size of Co_3O_4 particles was determined. Average particle sizes are listed in Table 3.1 (page 28). As this is a non-bulk technique, the actual average over all particles might be different from this average of randomly selected Co_3O_4 particles. Furthermore, particles with a size lower than the resolution (about 1 nm) are too small to be seen, increasing the observed average particle size if sub-resolution particles are present. Figures 3.3–3.90 represent a selection of TEM images.

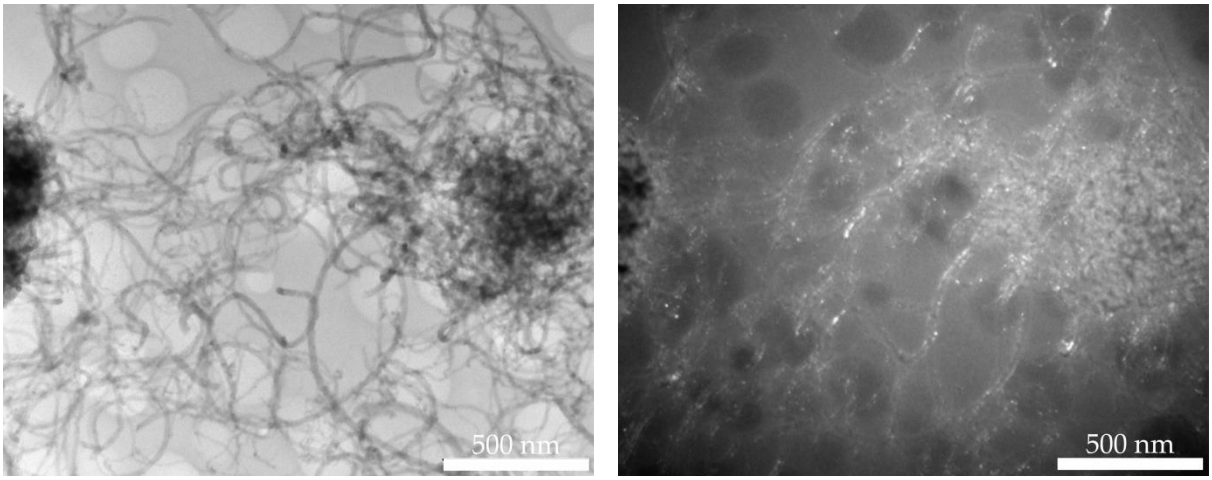

Figure 3.3 Bright field (left) and HAADF image of catalyst CNT-PrOH-2. The images were acquired at the same location.

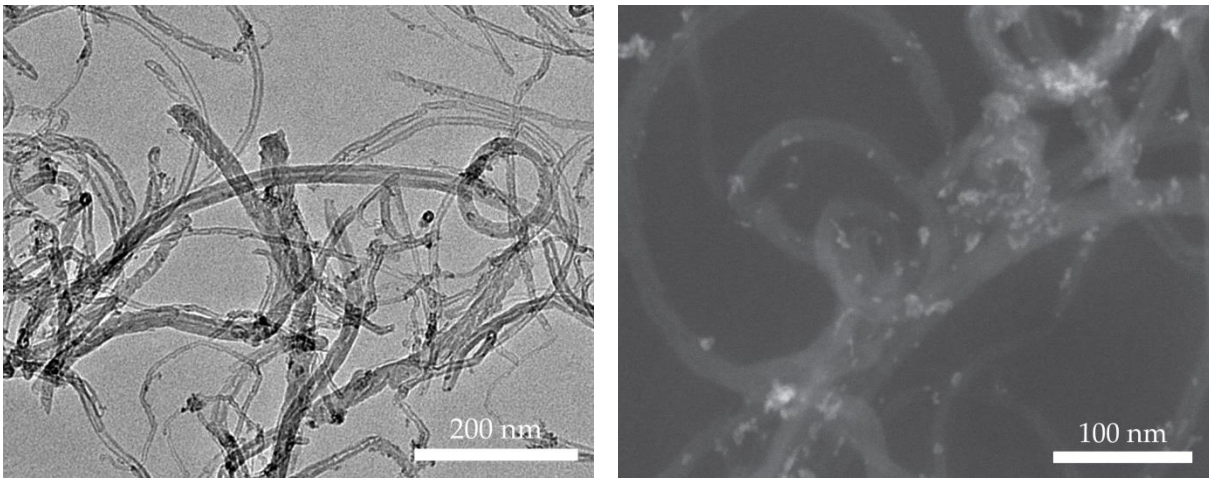

Figure 3.4 Bright field (left) and HAADF image of catalyst CNT-PrOH-3.

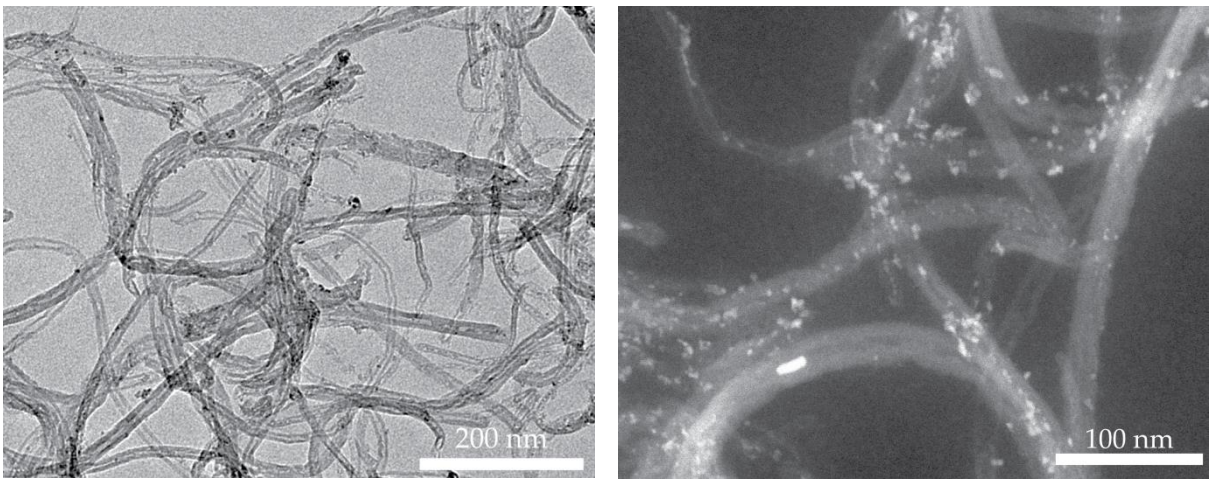

Figure 3.5 Bright field (left) and HAADF image of catalyst 2hGPO-PrOH-2. The bright particle inside a tube in the HAADF image is a trace of the growth catalyst.

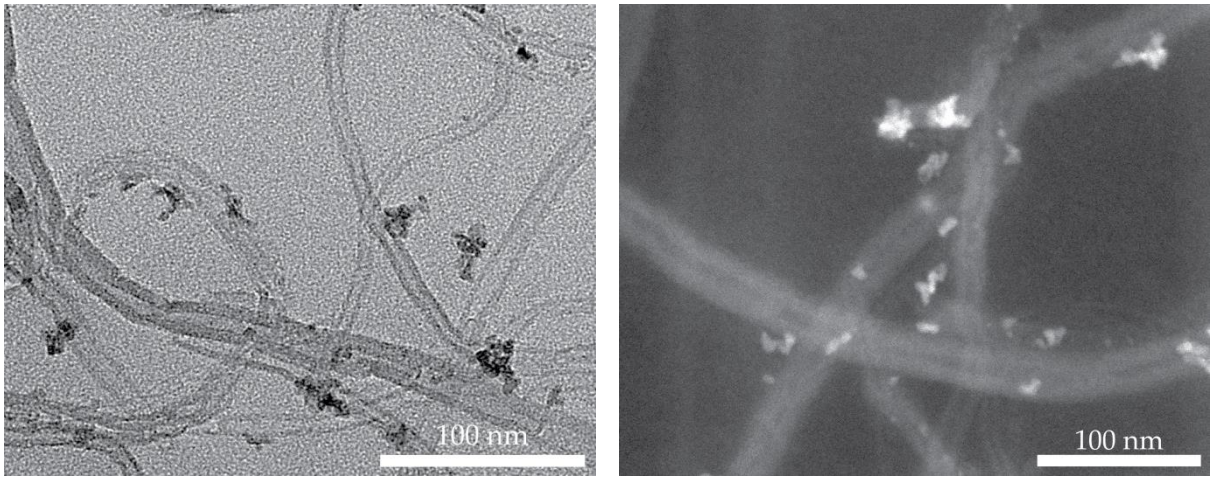

Figure 3.6 Bright field (left) and HAADF image of catalyst CNT-EtOH-6

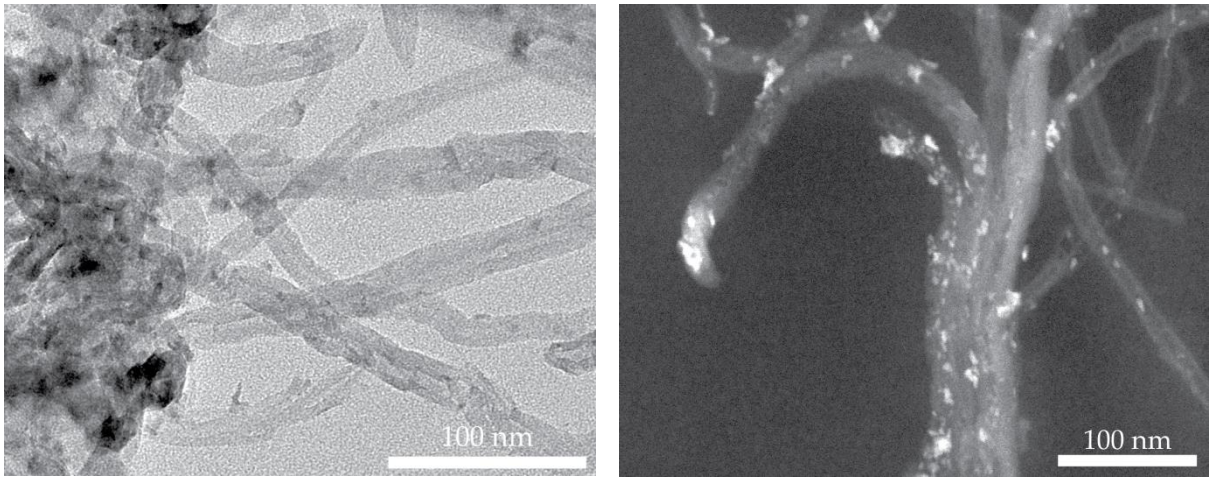

Figure 3.7 Bright field (left) and HAADF image of catalyst 2hGPO-EtOH-1

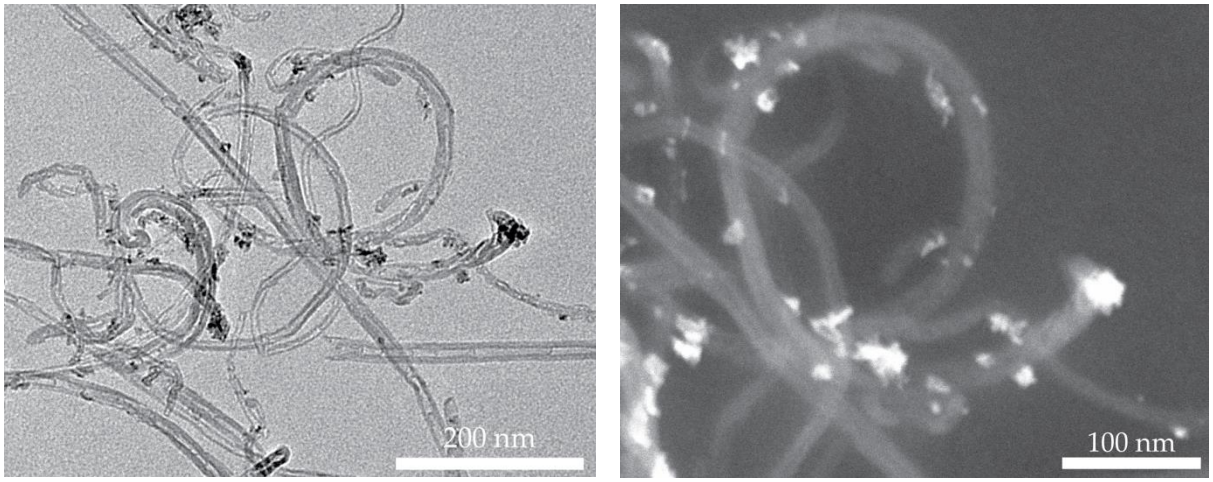

Figure 3.8 Bright field (left) and HAADF image of catalyst CNT-H2O-1

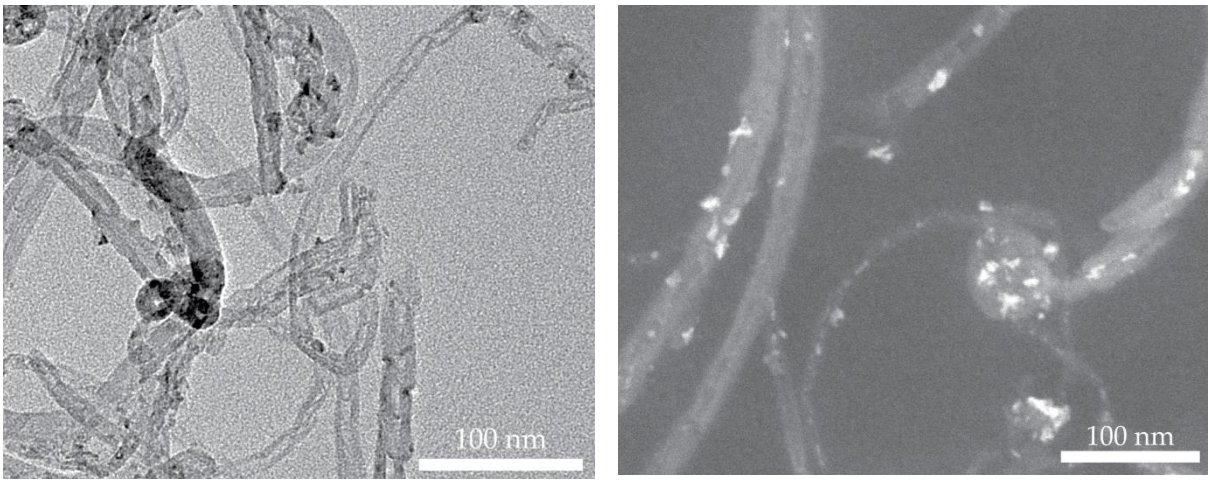

Figure 3.9 Bright field (left) and HAADF image of catalyst 2hGPO-H2O-1

In all images it is seen that the shape of Co_3O_4 particles is not well defined. The average particle size is near 5 nm. The different preparation methods have not lead to different Co_3O_4 crystallite sizes. The catalysts where ethanol or 1-propanol was used as impregnation solvent show better particle distribution than water impregnated catalyst CNT-H2O-1.

An important difference between the water-impregnated catalysts CNT-H2O-1 (Figure 3.8) and 2hGPO-H2O-1 (Figure 3.9) is the distribution of the Co_3O_4 particles. In catalyst CNT-H2O-1, the particles appear to be clustered and the sample seems to be free of isolated particles, whereas catalyst 2hGPO-H2O-1 does have these isolated particles. The difference between CNT-H2O-1 and 2hGPO-H2O-1 can be ascribed to the wetting of the surface: for CNT-H2O-1, untreated CNT were used which are hydrophobic and the impregnation solution was therefore not able to fully wet the surface, creating clustered particles. Catalyst 2hGPO-H2O-1 was prepared from GPO treated CNT and therefore had a hydrophilic surface prior to impregnation, leading to a better particle distribution.

The absence of structural differences as a result of the preparation method was also recognized from the XRD patterns. Typical XRD patterns are shown in Figure 3.10.

It is seen that the GPO treatment did not significantly influence the XRD patterns. Untreated CNT and 0.5 h GPO CNT show the same signals at comparable relative intensities. The same holds for catalysts CNT-PrOH-3, CNT-EtOH-6, CNT-H2O-1, 2hGPO-PrOH-1, 2hGPO-EtOH-1, 2hGPO-H2O-1 and R2hGPO-PrOH-1. Furthermore, the size of the particles seems not to be dependent on the support surface treatments.

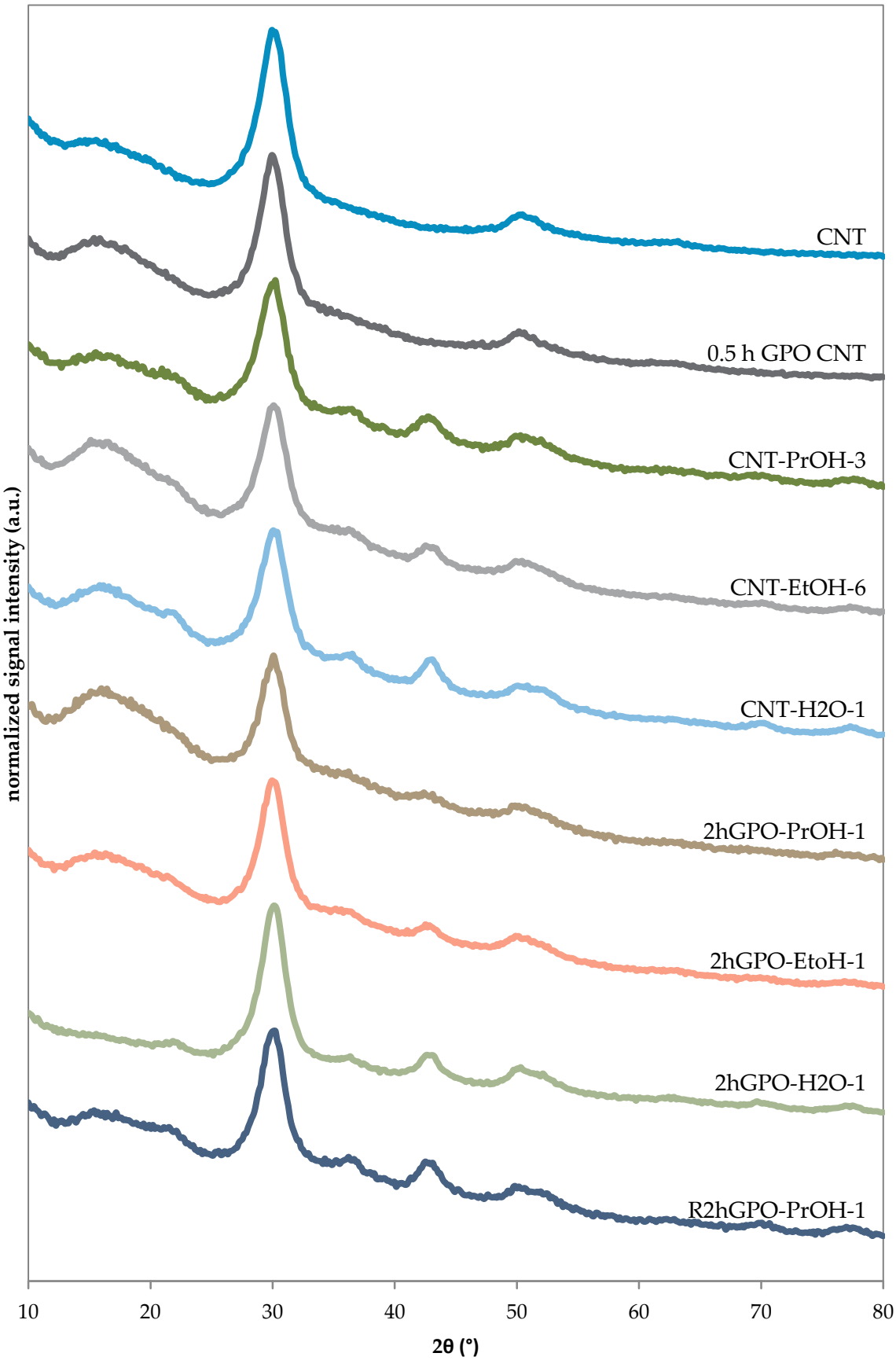

Figure 3.10 XRD patterns for fundamentally different catalysts. The peaks near 36° and 43° are assigned to Co_3O_4.

The equivalent Co crystallite sizes were estimated by applying Equation (3.5) on the XRD Co_3O_4 particle size and are shown in Table 3.1 (page 28). The surface area and active site density were estimated using Equation (4.9) and are shown in Table 3.3.

Hydrogen chemisorption curves (first analysis) for catalysts CNT-PrOH-2 and 0.5hGPO-PrOH-2 are plotted in Figure 3.11. From the observed pattern (rapid adsorption at low pressure and then reaching equilibrium) it is concluded that hydrogen chemisorption is a suitable technique to characterize Co/CNT catalysts. The particle sizes as determined from chemisorption are shown in Table 3.1 on page 28.

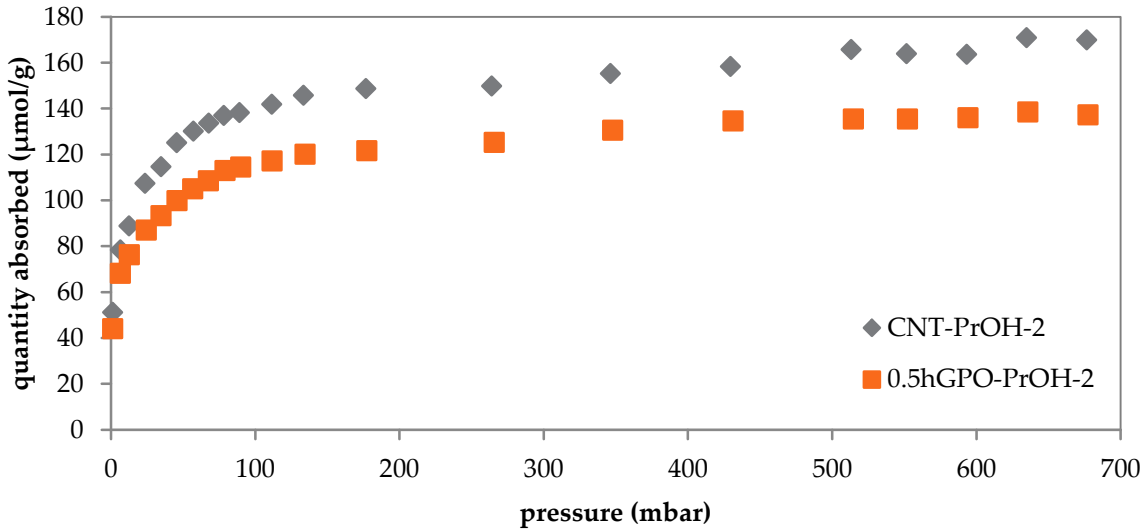

Figure 3.11 Hydrogen chemisorption curves of catalysts CNT-PrOH-2 and 0.5hGPO-PrOH-2.

The accessible surface area and active sites density are shown in Table 3.3. As expected from the chemisorption curves where CNT-PrOH-2 has a higher quantity adsorbed than 0.5hGPO-PrOH-2 despite similar Co loading, the metal surface area of catalyst CNT-PrOH-2 is higher than catalyst 0.5hGPO-PrOH-2.

Table 3.3 Accessible surface area and active sites density determined by hydrogen chemisorption and estimated by applying Equation (4.9). For the calculation of the active sites density, a cobalt atomic surface area of 6.62 Å^2 was used.

	accessible surface area (m^2/g_{Co})		active sites ($mmol/g_{Co}$)	
Catalyst	**X-ray diffraction**	**H_2 chemisorption**	**X-ray diffraction**	**H_2 chemisorption**
CNT-PrOH-1^P	140.4		3.5	
CNT-PrOH-2	124.8	126.4	3.1	3.2
CNT-PrOH-3	112.6		2.8	
0.5hGPO-PrOH-2	115.2	100.2	2.9	2.5
2hGPO-PrOH-1	91.72		2.3	
2hGPO-PrOH-2	133.0		3.3	
0.5hGPO-PrOH-1	104.5		2.6	
R0.5hGPO-PrOH-1	89.89		2.3	
R2hGPO-PrOH-1	103.6		2.6	
4hGPO-PrOH-1	102.6		2.6	
CNT-EtOH-5	107.3		2.7	
CNT-EtOH-6	101.7		2.6	
CNT-H2O-1	79.41		2.0	
2hGPO-EtOH-1	98.78		2.5	
2hGPO-H2O-1	87.78		2.2	

^{P} catalyst was reduced and passivated after thermal treatment

From Table 3.3 it is seen that the surface area estimation by using XRD is in reasonable accordance with the data obtained by H_2 chemisorption where it was studied.

3.3.3 Reducibility and thermal stability

The reducibility of several catalysts was investigated by temperature programmed reduction (TPR) experiments. Results from TPR experiments are shown in Figure 3.12. Both steps of the two-step reduction and the hydrogen uptake by the support occur at higher temperatures when the support is GPO treated. The peak for the hydrogen uptake by the support of these catalysts is shifted to low temperature compared to the TPR experiment on a GPO treated support sample without metal loading (Figure 2.4).

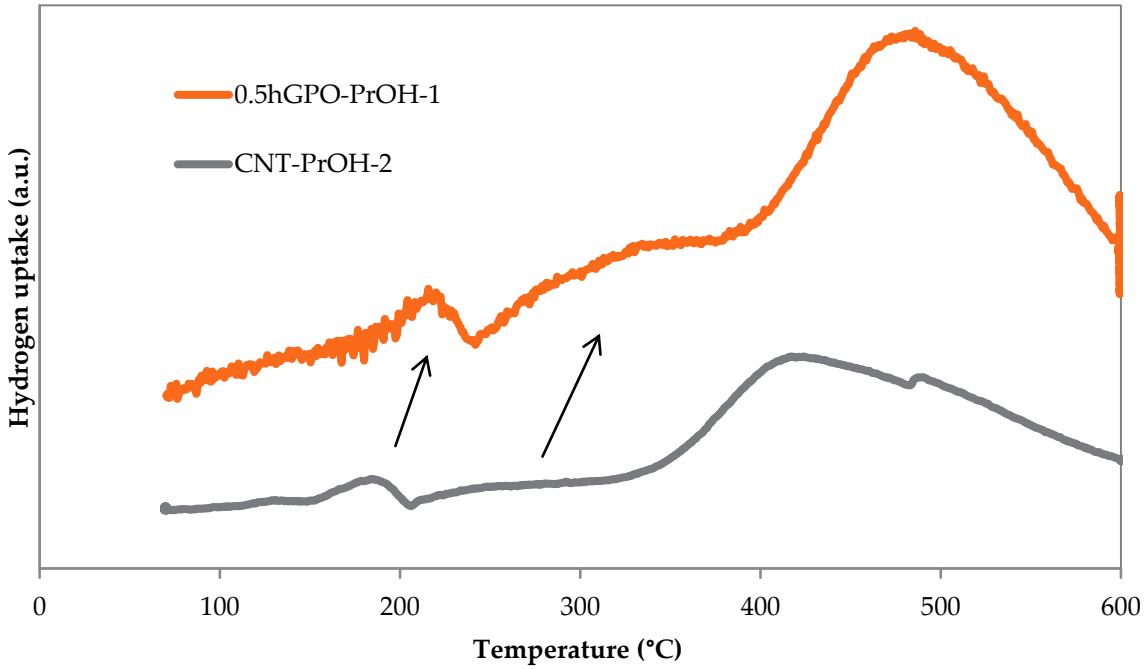

Figure 3.12 Results of the TPR analyses of catalysts CNT-PrOH-2 and 0.5hGPO-PrOH-1 and a 1.25 h GPO treated CNT sample. The temperature ramp was 2 °C/min. Another TPR experiment on catalyst 0.5hGPO-PrOH-1 with a different ramp rate of 5 °C/min is plotted for comparison. At this higher ramp rate, less time is available for the particles to reduce and therefore, the signals are stronger and appear at higher temperature.

When cobalt is supported on a strongly interacting support such as titania, the reduction temperature is lower [67]. As mentioned before, the binding strength between oxidized CNT and copper is higher than the binding strength between untreated CNT and copper [50]. If this would be the case for cobalt as well, the reduction temperature offset is expected to be lower for cobalt on the GPO treated CNT than for cobalt on untreated CNT.

In fact, Yu *et al.* [68] found that Co_3O_4 particles supported on oxidic carbon nanofibers (equivalent Co size 12 nm) are reduced at lower temperature than Co_3O_4 particles supported on non-oxidic carbon nanofibers (equivalent Co size 36 nm). Apparently, this is not the case for the catalyst systems used in this research. A possible explanation could be an effect of the particle size on the reduction temperature. Metal nanoparticles have a higher reduction temperature offset than bulk metal. For Co on SiO_2 (which is a non-reducible support), Den Breejen found that smaller particles need a higher reduction temperature in order to obtain the same reduction degree [69]. However, as the equivalent Co particle sizes of CNT-PrOH-2 and 0.5hGPO-PrOH-1 before reduction are 2.7 nm and 3.2 nm, as determined by XRD, this does not explain the reduction behavior. The last explanation is the possibility that oxygen groups on the CNT support are able to oxidize metallic cobalt, slowing down the reduction process.

The overlap between the second peak where CoO is reduced to Co and the hydrogen uptake by the support makes a quantitative comparison based on TPR data alone impossible.

The thermal stability of 2hGPO-PrOH-1 was determined by a TGA experiment and is presented together with a TGA pattern of INE8 in Figure 3.13. The difference between the two catalyst samples is negligible. The sudden jump at a temperature of 550 °C is assigned to the loss of non-graphitic carbon [56], [70]. Comparing these patterns to the ones in Figure 2.8, it is recognized that the presence of cobalt alters the thermal behavior: support samples without metal do not show the sudden jump at a temperature of 550 °C.

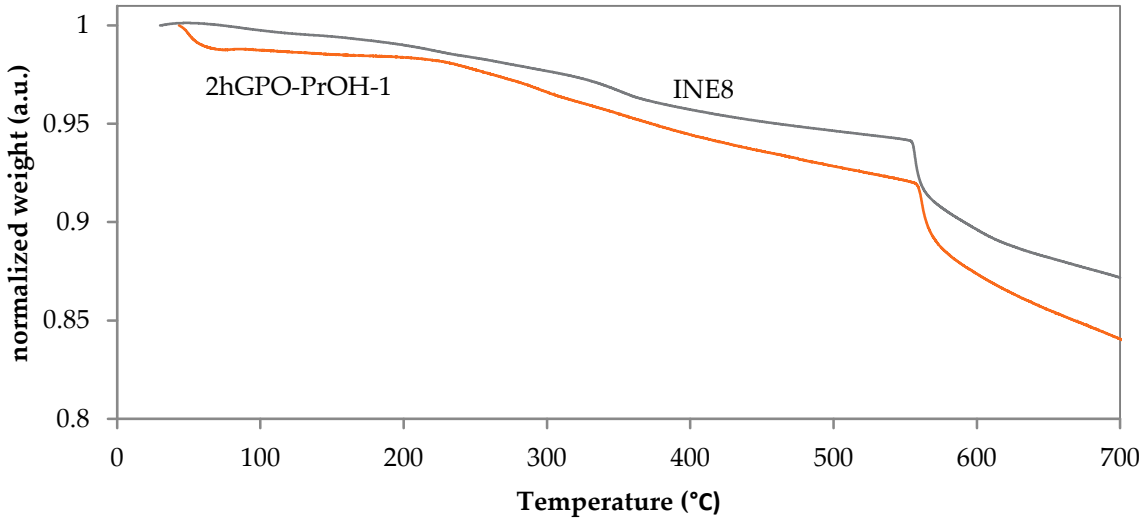

Figure 3.13 TGA data for samples 2hGPO-PrOH-1 (bottom) and INE8 by René Manchester (top). 2hGPO-PrOH-1 was analyzed by increasing the temperature from 50–700 °C at a ramp rate of 5 °C/min, in a 20 mL/min nitrogen flow, INE8 was held at 30 °C for 20 min after which the temperature was increased to 700 °C at the same ramp rate in a 20 mL/min argon flow.

The TGA measurement for catalyst INE8 was measured with an on-line mass spectrometer (MS), analyzing the product gases. The removal of carbon is confirmed by the MS data plotted in Figure 3.14. The samples lose carbon in the forms of carbon dioxide and elementary carbon at low temperatures, and at the sudden jump at T=550 °C, also carbon monoxide and oxygen are recognized.

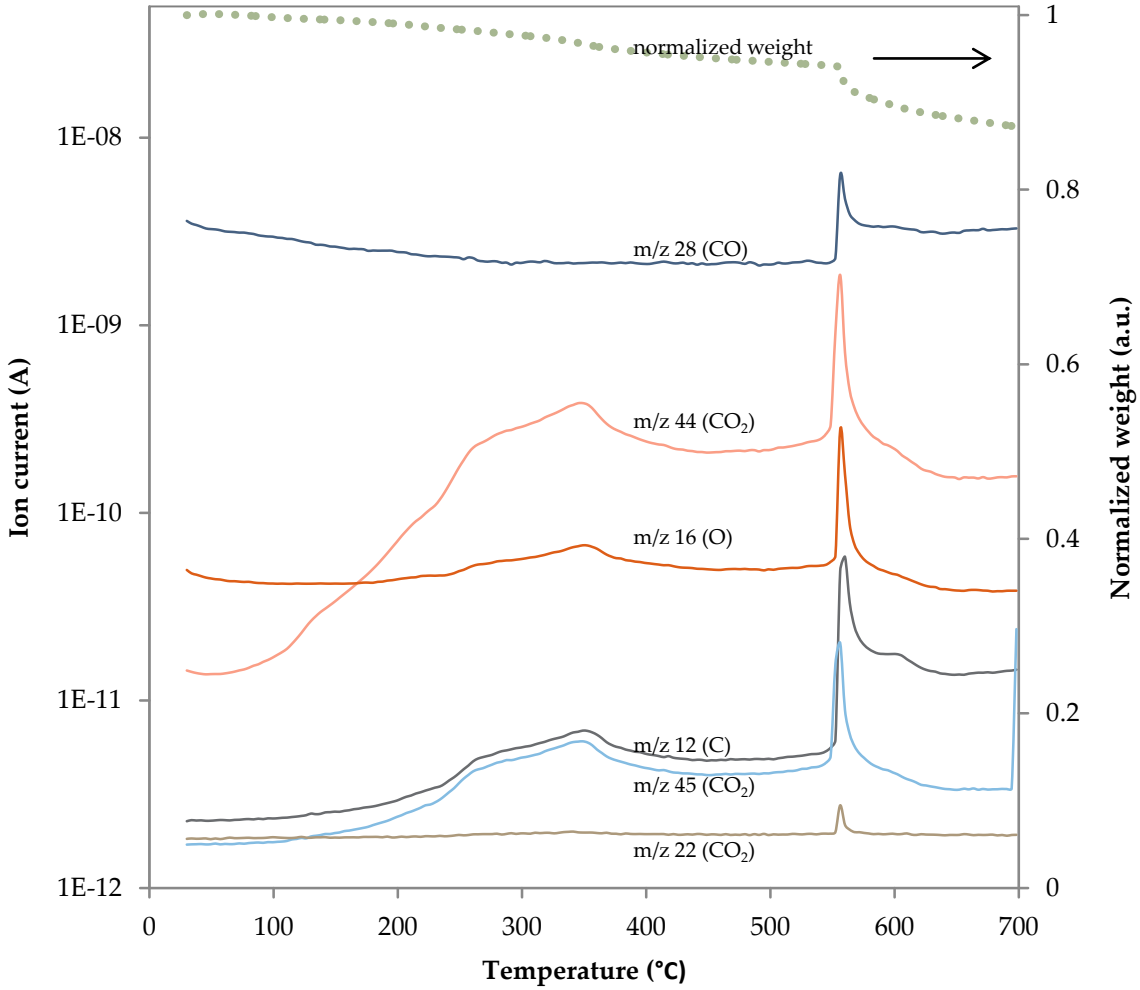

Figure 3.14 TGA-MS data for INE8 by René Manchester (8% Co, ethanol impregnated CNT, dried overnight at 120 °C in static air). This measurement is identical to the one shown in Figure 3.13.

3.4 Summary and outlook

Cobalt catalysts have been prepared by incipient wetness impregnation of solutions of cobalt nitrate hexahydrate in water, ethanol and 1-propanol, supported on CNT, GPO treated CNT and reduced GPO treated CNT. After impregnation, the samples were dried in a nitrogen flow at either 60 °C (for the ethanol samples) or 80 °C (for the water and 1-propanol samples) and subsequently thermally treated at 250 °C to yield supported Co_3O_4 particles. The Co weight loading was near 10%. From TGA measurements it was seen that the catalyst samples have high thermal stability in an inert atmosphere.

In general, the surface treatment or impregnation solvent did not have a significant influence on the structural appearance as determined by XRD and TEM. However, when using water as impregnation solvent, isolated particles were visible on the GPO treated support, but not on the untreated support. This is explained by the hydrophobicity of untreated CNT

and the hydrophilic character of GPO treated CNT. The difference between the two types of support material were not seen when ethanol or 1-propanol were used as impregnation solvent. Just like these alcohols can dissolve both polar and non-polar compounds, they are able to wet the surface independent of surface oxygen groups.

The cobalt equivalent crystallite sizes were determined by hydrogen chemisorption and calculated by applying a molar volume correction factor on the Co_3O_4 crystallite size determined by TEM and by applying the Debye-Scherrer equation on XRD patterns. The values determined by XRD (2.4–4.2 nm) and TEM (3.3–4.3 nm) were in reasonable accordance, although the TEM measurements were slightly higher. This was explained by the fact that TEM is a non-bulk technique whereas XRD is a bulk technique. Therefore, in TEM only a number of randomly selected particles was used to calculate the average particle size. It is obvious that sub-resolution particles were not taken into account. Another explanation can be found in the inaccuracy of the Debye-Scherrer equation, which assumes the particles are spherical. The particle sizes of different systems were too similar to find an influence of the impregnation solvent or support pre-treatment.

The accessible metallic surface areas were determined by hydrogen chemisorption in two cases. The catalyst on a GPO treated support had a lower accessible metal surface area than the catalyst on an untreated CNT support, but with only two samples measured it is impossible to reveal a trend. To have insight into the metal surface area of all catalyst samples, an estimation was made based on the Co crystallite size determined by XRD. This estimation was in reasonable accordance with the cobalt surface area obtained from hydrogen chemisorption where it was measured.

The reduction temperature of cobalt supported on GPO treated CNT was higher than for cobalt on untreated CNT, as determined by TPR. This was explained by the oxidative capability of the oxygen groups on the support.

Further analyses are necessary to find the influence of the system on its reducibility. The products formed during the TPR analysis can be analyzed by an online mass spectrometer coupled to the TPR setup and the reduction process can be monitored by *in situ* XRD. Furthermore, the influence of the support type to the reduction behavior of the cobalt oxide particles can be investigated by temperature programmed X-ray Absorption Near Edge Structure (XANES) or Extended X-ray Absorption Fine Structure (EXAFS) [69], [71].

More accurate determinations of the metal surface area are necessary for further explanation of catalyst behavior. The calculations were based on the cobalt equivalent particle size as determined by XRD. As the patterns were recorded *ex situ* before catalysts have been tested, the calculated metal surface areas were likely off in some cases: especially in the case of the catalysts with the clustered metal particles. Further chemisorption analysis are necessary.

Chapter 4

Testing the catalysts in the FTS

The catalytic FTS performance of the catalysts prepared in the previous chapter was investigated at both ambient and high (20 bar) pressure. The experimental procedure is described in Section 4.1. Sections 4.2 and 4.3 cover the results from the tests at ambient and high pressure, respectively and the spent catalysts are characterized by TEM in section 4.4.

The possible promoting effect of manganese traces in the CNT will be checked by comparing catalytic performance data of Co/CNT with Co on Ni grown carbon nanofibers, promoted with different amounts of manganese.

4.1 Experimental

4.1.1 Ambient pressure

For the ambient pressure tests, a 20 mg catalyst sample was diluted with 200 mg SiC (0.2 mm) and loaded into a glass plug flow reactor. The reactor was mounted in an oven (fixed bed). The sample was reduced at 350 °C (ramp rate 5 °C/min) in a flow of 36 mL/min Ar and 4 mL/min H_2. After cooling down to 220 °C, the gas flow was changed to 12 mL/min H_2 and 6 mL/min CO. The product composition was analyzed every hour by an online gas chromatographer (Varian 430-GC with a fused silica CP—Sil 5CB column, products quantified with an FID).

4.1.2 High pressure

High pressure tests were performed in an Avantium Flowrence unit in which 16 stainless steel reactors run in parallel. The system was equipped with an online GC (Agilent Technologies 7890A). Permanent gases are separated in a micropacked ShinCarbon ST (#19043) column and quantified with a TCD. The hydrocarbon products (C_1–C_9) are separated on an Agilent J&W PoraBOND Q column, analyzed with a FID and quantified against the TCD signal of the internal standard He.

The reactors were loaded with an undiluted catalyst sample of 35–40 mg (about 200 μL), using particles within the size range 90–212 μm. The catalysts were dried in flowing heluim at 100 °C (ramp rate 10 °C/min) and subsequently reduced in situ in a flow of H_2/He (1:3, v/v) at 350 °C (ramp rate 1 °C/min) for 8 h. The temperature was lowered to 180 °C (ramp

rate 3 °C/min) and pressurized to 20 bar. After switching to syngas (H_2:CO ratio 2:1), the temperature was increased to 220 °C at 1 °C/min. The influence of the amount of catalyst in the reactor was investigated by a lower catalyst loading (12 mg) and by diluting the 35-40 mg sample with 150 mg SiC (grain size 0.2 mm)

To investigate the thermal stability of the catalysts, the reactor temperature was increased to 250 °C in steps of 10 °C, and then lowered to 220 °C. To get insight into the reversibility of the deactivation, a 16 h treatment by diluted hydrogen was performed at 300 °C after a steady state was reached [44].

4.1.3 Definitions

By varying the volumetric feed flow rate, the influence of residence time can be investigated This rate is described in terms of the gas hourly space velocity (GHSV) relating the gas flow into the reactor to the volume of the catalyst [72]. The GHSV reported is calculated based on a catalyst loading of 200 μL, in all cases:

$$GHSV\ (\mathrm{h}^{-1}) = \frac{\dot{V}_{\mathrm{feed}}}{V_{\mathrm{catalyst}}} \tag{4.1}$$

Selectivity

In catalysis research, the selectivity of the catalyst is an important parameter. For the high pressure tests, the selectivity was calculated following Equation (4.2) [1]:

$$S_{\mathrm{C}_n}\ (\mathrm{carbon\%}) = \frac{n \times \mathrm{moles\ C}_n\ \mathrm{formed}}{\mathrm{moles\ CO\ converted}} \times 100\% \tag{4.2}$$

For the tests at ambient pressure, the selectivity was calculated in a similar way:

$$S_{\mathrm{C}_n}\ (\mathrm{carbon\%}) = \frac{n \times c_{\mathrm{C}_n}}{\sum_m m \times c_{\mathrm{C}_m}} \times 100\% \tag{4.3}$$

Hydrocarbons up to a length of 18 were included in this calculation. Low pressure C_{5+} selectivity was calculated as

$$S_{\mathrm{C}_{5+}}(\mathrm{carbon\%}) = \sum_{n=5}^{18} S_{\mathrm{C}_n} \tag{4.4}$$

This way, all products up to C_{18} are included in the calculations.

For the high pressure tests, the C_{5+} selectivity was determined indirectly, assuming only hydrocarbons have been formed:

$$S_{\mathrm{C}_{5+}}(\mathrm{carbon\%}) = 100\% - \sum_{n=1}^{4} S_{\mathrm{C}_n} \tag{4.5}$$

Product distribution

The α value was determined by plotting $\log_{10} W_n/n$ for each carbon number n and then applying a linear fit (like $y = bn + c$). Rewriting Equation (1.5) as Equation (4.6) it is seen that $\alpha = 10^b$. The linear fit was applied in the range [4,7] for the high pressure tests. In the ambient pressure tests, the range was [4,11].

$$\log\frac{W_n}{n} = n\log\alpha + [2\log(1-\alpha) - \log\alpha] = n\log\alpha + \text{const.} \tag{4.6}$$

Activity

The number of conversions per surface metal atom per second, or turnover frequency (TOF):

$$\frac{\text{CO converted } (\text{mL}_\text{n}/\text{min})}{60\ \text{s/min} \times 22414\ \text{mL}_\text{n}/\text{mol}} \Big/ \text{number of surface metal atoms (mol)} \tag{4.7}$$

The amount of CO converted per unit mass of cobalt per second, or cobalt time yield (CTY):

$$CTY = \frac{\text{moles CO converted}}{m_{\text{Co}} \times \text{time}} \tag{4.8}$$

Cobalt surface area per unit mass was estimated by the following formula:

$$\frac{\text{accessible Co surface area}}{\text{unit mass}} \cong \frac{1}{2} \cdot \frac{\text{surface per Co particle}}{\text{mass per Co particle}} = \frac{1}{2} \cdot \frac{4\pi r^2}{\frac{4}{3}\pi r^3 \rho} \tag{4.9}$$

In this equation, r is the average radius of the Co particles and ρ is the bulk density of the metal. The factor ½ accounts for the fact that the surface is not fully accessible, for instance due to binding to the tubes, and the surface might decrease due to net particle growth during the reduction step (which has not been carried out yet before the particle size determination).

Activation energy

The activation energy E_a can be determined from the Arrhenius equation (Equation (4.10)) [73]. In this equation, k is the reaction rate constant, R is the ideal gas constant (8.314 J mol^{-1} K^{-1}), T is the reaction temperature, x_{CO} is the fraction of CO that is converted and A is a constant. Through Equation (4.11) it is seen that the E_a can be determined from an Arrhenius plot by plotting the natural logarithm of k as a function of T^{-1} and applying a linear fit (Equation (4.12)). The activation energy is then calculated by applying Equation (4.13).

$$k = Ae^{-\frac{E_a}{RT}} \propto \ln(1 - x_{\text{CO}}(T)) \tag{4.10}$$

$$\ln k \propto \frac{E_a}{RT} \tag{4.11}$$

$$\ln k = aT^{-1} + b \tag{4.12}$$

$$E_a = a/R \tag{4.13}$$

4.2 Testing results: ambient pressure

The results of catalytic tests at ambient pressure are summarized in Table 4.1. At this pressure, the selectivity towards higher hydrocarbons is very low compared to earlier and other work [56], [61]. Furthermore, the catalysts are highly active compared to these other studies while the CO conversion is similar. When comparing the activity of the catalysts from this work, the catalysts supported on untreated CNT exhibit higher activity than those on GPO treated or reduced GPO treated CNT.

The performance of catalyst CNT-PrOH-1 is about 50% lower than the performance of catalyst CNT-PrOH-2. A likely explanation for this behavior is the additional reduction of CNT-PrOH-1 which was followed by a passivation step directly after the thermal treatment. During the reduction, the temperature is well above the Hüttig temperature (Equation (1.6)) and the cobalt atoms are therefore mobile, especially those on edge sites and defect sites. The metal particles can thus grow during the reduction and form new (larger) crystallites. The passivation step is meant to protect the metal particles from air exposure, but does partially oxidize the cobalt crystallites, forming new edge and defect sites that become mobile during the second reduction step. Therefore, even less cobalt atoms are exposed to the surface, yielding a lower activity per unit mass of metal.

Table 4.1 Steady state performance for testing at 220 °C at atmospheric pressure, H_2:CO=2

catalyst	CTY (10^{-5} mol CO/(g $_{Co}$/s))	CO conversion (%)	C_1 selectivity (carbon%)	C_{5+} selectivity (carbon%)	ASF: α
CNT-PrOH-1[r]	4.2	1.6	58	12	0.58
CNT-PrOH-2	8.1	3.2	61	12	0.53
0.5hGPO-PrOH-1	6.7	3.1	57	15	0.58
2hGPO-PrOH-1	5	2	60	13	0.53
4hGPO-PrOH-1	6.4	2.7	57	14	0.56
R0.5hGPO-PrOH-1	6.8	3.1	58	14	0.57
R2hGPO-PrOH-1	7.4	3.3	61	13	0.56

[r] Catalyst received an additional reduction followed by passivation directly after the thermal treatment.

As stated in Section 2.1, the CNT used in this work have high purity, but traces of the growth catalyst might still be present. Indeed, the untreated CNT contain some cobalt particles which are located inside the tubes [56]. Performing catalytic tests on untreated CNT has

proven that these particles have no influence on activity: the CTY of these unloaded catalysts is zero. However, as was also stated, the CNT might also contain traces of Mn.

Table 4.2 Steady state performance of Mn promoted Co on nickel grown CNF (liquid phase oxidized) at 220 °C and atmospheric pressure (taken from Leendert Bezemer [46]). The sample names denote the Co:Mn atomic ratio. First, cobalt was loaded on the CNFs followed by manganese. CoH was impregnated with a diluted nitric acid solution and does not contain any manganese.

Sample	CTY (10^{-5} mol CO/g_{Co}/s)	TOF (10^{-3} s^{-1})	C_1 selectivity (wt%)	C_{5+} selectivity (wt%)	ASF: α
CoH	1.8	14	36	31	0.60
Co431Mn	1.7	13	32	36	0.63
Co95Mn	1.8	17	28	41	0.65
Co39Mn	1.6	16	25	45	0.67
Co19Mn	1.4	13	25	44	0.66
Co11Mn	1.2	11	23	45	0.67

From Table 4.2 it is seen that using a Mn promoted catalyst, the C_{5+} selectivity and α value increase with increasing Mn content. The catalysts supported on GPO treated CNT from this research are expected to have a lower Mn loading compared to the catalysts supported on untreated CNT, if at all. There is no clear trend in C_{5+} selectivity and α between the tests of different catalysts from this research as seen in Table 4.1. Therefore, an effect of Mn promotion coming from impurities in the CNT is thought to be negligible.

4.3 Testing results: high pressure

The results of the high pressure tests are summarized in Table 4.3. The results are explained in the following sections. Section 4.3.2 covers the influence of oxygen containing groups on the support surface and structural damage to the support surface. Section 4.3.3 describes the influence of the solvent used in the impregnation step. Section 4.3.4 provides some insight into the deactivation mechanism. The product distribution is explained in Section 4.3.5 and the activation energy is determined in Section 4.3.6.

It was seen that catalysts from different batches have comparable performance. However, catalysts from the same batch have different performance between runs. The design of the setup in which a total gas flow is divided over the 16 reactors is such that the actual gas flow can be slightly different from the desired gas flow. Another reason could be a different pressure drop over the reactors when different types or amounts of catalysts are used. However, no significant difference was found when measuring the flow through the 16 reactors when

the reactors were filled with different types and amounts of catalysts or related materials. Furthermore, catalyst samples can be inhomogeneous. However, as all catalysts were sieved prior to the runs, this is unlikely. Because of the difference in performance between runs, only comparisons within single runs are made.

4.3.1 General

Apparent turnover frequencies were determined from the accessible surface area as determined from the particle size as obtained from XRD analysis (Table 3.3).

The catalysts showed a relatively high performance (CTY and apparent TOF) and high selectivity towards higher hydrocarbons (above 80%, compared to Co/CNF at 74% [46]). When measuring under the same conditions, 10 wt% Co/TiO_2 has a CTY of $5–11\times10^{-5}$ mol $CO/g_{Co}/s$, depending on the preparation method (interpolated from [74]), 11% Co/Nb_2O_5 has a CTY of 5×10^{-5} mol $CO/g_{Co}/s$ [75]. The high CTY was noticed before for Co/CNT catalysts [56].

Table 4.3 Steady state performance for testing at 220 °C at 20 bar pressure, H_2:CO=2, GHSV=2000 h^{-1}, values shown are averaged over the last five data points before 84 h (run 2: 143 h) time on stream.

catalyst	run number	CTY (10^{-5} mol CO/g_{Co}/s)	apparent TOF (10^{-3} mol_{CO}/$mol_{active\ sites}$/s)	CO conversion (%)	C_1 selectivity (carbon%)	C_2–C_4 selectivity (carbon%)	C_{5+} selectivity (carbon%)	ASF: α
CNT-PrOH-2	1	22	71	48	17	19	64	0.68
CNT-PrOH-2	1	21	67	53	16	22	62	0.68
CNT-PrOH-2 [a]	2	20	64	14	8	8	84	0.64
CNT-PrOH-2	4	22	71	42	8	8	83	0.74
CNT-PrOH-2	4	22	70	44	9	8	83	0.74
CNT-PrOH-3	3	15	52	37	6	6	88	0.78
CNT-PrOH-3	4	20	69	41	8	8	84	0.75
CNT-PrOH-3[a]	4	19	67	14	10	9	81	0.72
CNT-PrOH-3[b]	4	20	70	42	8	8	84	0.75
CNT-PrOH-3	4	20	71	46	8	8	84	0.75
CNT-PrOH-4	4	22	ND	48	8	7	85	0.76
CNT-EtOH-6	3	17	69	42	5	5	90	0.80
CNT-H2O-1	3	12	62	29	5	4	91	0.80
0.5hGPO-PrOH-2	1	12	41	33	19	24	57	0.59
0.5hGPO-PrOH-2 [a]	2	15	51	11	8	7	85	0.62
2hGPO-PrOH-1	1	14	59	42	17	19	64	0.62
2hGPO-PrOH-1	2	12	52	25	7	7	87	0.70
2hGPO-PrOH-2	3	8	24	20	10	7	83	0.74
2hGPO-PrOH-2	4	12	35	27	10	9	81	0.71
2hGPO-PrOH-2[a]	4	12	37	9	11	10	78	0.66
2hGPO-PrOH-2[b]	4	11	32	24	10	9	81	0.70
2hGPO-PrOH-2	4	12	35	27	10	9	81	0.71
4hGPO-PrOH-1	1	12	48	37	21	25	55	0.62
4hGPO-PrOH-1	4	13	51	28	10	8	83	0.73
4hGPO-PrOH-1	2	11	41	27	7	7	86	0.71
2hGPO-EtOH-1	3	8	33	21	10	7	82	0.74
2hGPO-H2O-1	3	7	30	16	11	7	82	0.76
R0.5hGPO-PrOH-1	1	18	78	49	18	20	62	0.63
R0.5hGPO-PrOH-1	2	13	57	25	6	7	87	0.68
R2hGPO-PrOH-1	1	17	67	43	21	21	57	0.62
R2hGPO-PrOH-1	2	8	30	21	7	7	86	0.66

[a] Low catalyst loading (12 mg)

[b] Diluted with 150 mg SiC (0.2 mm)

4.3.2 Influence of oxygen groups

From Figure 4.1 it is seen that catalysts supported on GPO treated CNT show lower activity than those supported on untreated CNT. This trend is the same as in the ambient pressure tests, however the difference is more pronounced in these high pressure tests.

The data points shown are averaged over six data points due to severe scattering. This scattering was caused by damage to the GC column. For the catalysts supported on reduced GPO treated supports (R0.5hGPO-PrOH-1 and R2hGPO-PrOH-1), the activity was higher than the values found for the catalysts supported on GPO treated CNT but still below the untreated CNT supported catalyst CNT-PrOH-2. From this run, no clear correlation between oxidation time and activity loss was found. However, as the column of the GC was damaged, the actual performance of the catalysts might differ from the data obtained from the GC. Therefore, this run was repeated after the GC column was repaired. Results of this second run are shown in Figure 4.2.

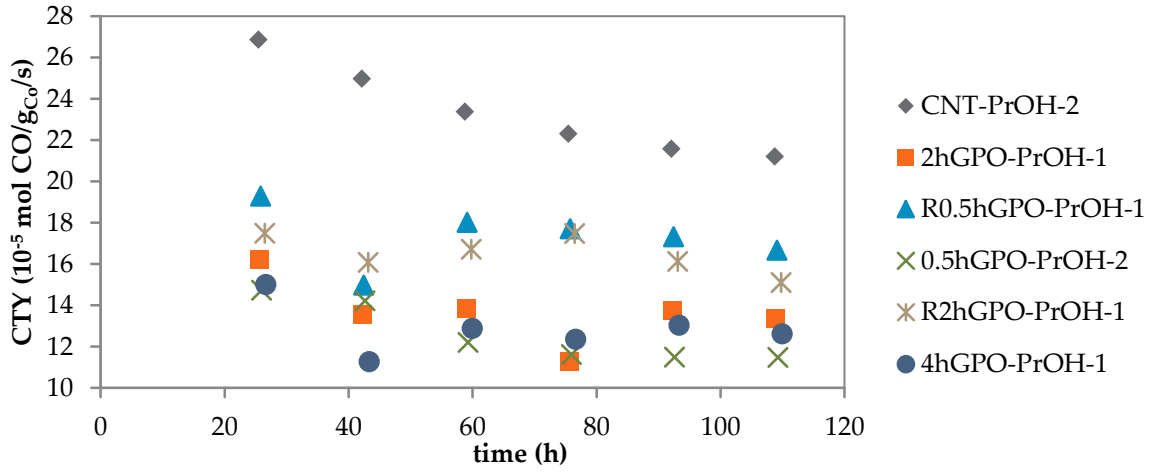

Figure 4.1 Activity of catalysts tested at 20 bar pressure and a temperature of 220 °C, run 1.

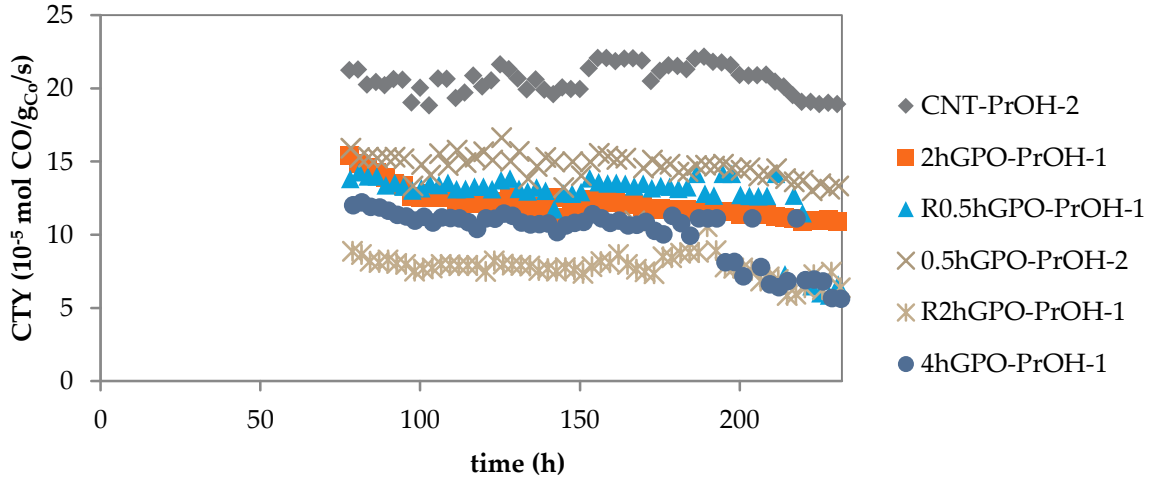

Figure 4.2 Activity of catalysts tested at 20 bar pressure and a temperature of 220 °C, run 2. The GHSV was changed from 2000 h^{-1} to 937 h^{-1} and 563 h^{-1} at 152.1 h and 185.4 h time on stream, respectively.

In run 2, for which the activity is plotted in Figure 4.2, the pressure of the reactors with catalysts 4hGPO-PrOH-1, R0.5hGPO-PrOH-1 and R2hGPO-PrOH-1 was unstable. Results for this run are therefore not fully representative. The data shown is somewhat scattered. This was caused by a lower reactor loading for some reactors due to limitations in catalyst availability. The lower loading caused the CO conversion to be low and thus the error in the measurements to be relatively large. However, as the CTY is a weight-based measure for the activity, a comparison between the catalysts can still be made. Again, it is seen that the catalyst CNT-PrOH-2 performs best, and catalysts supported on GPO treated CNT and reduced GPO treated CNT have a lower activity. The trend observed in Figure 4.1, where the performance of catalysts supported on reduced GPO treated CNT was in between the performance of those on untreated and GPO treated CNT is not confirmed in Figure 4.2.

4.3.3 Influence of the impregnation solvent

Figure 4.3 shows the activity expressed as CTY for 1-propanol, ethanol and water impregnated untreated and GPO treated CNT. Again, it is immediately seen that the activity of the catalysts supported on GPO treated CNT perform worse than those on untreated CNT. Using water as impregnation solvent leads to a lower activity for both the untreated and GPO treated CNT. As stated in Section 3.3.2, the particles were clustered when water is used as solvent. Clustered particles can combine during the reduction and thus grow, losing surface area and thus losing active sites. For the GPO treated CNT, no difference in activity is seen between the ethanol and 1-propanol impregnated samples, whereas for the untreated CNT the ethanol impregnated catalyst shows a significantly higher activity than the 1-propanol impregnated catalyst. The improved particle distribution observed for the alcohol impregnated catalysts combined with the particle size below the critical limit of 6 nm above which the turnover frequency is constant might play a role: when particles are smaller than 6 nm and do not grow to particles larger than 6 nm, the activity can be smaller than catalysts with larger particles [69], [76]. The spent catalysts were characterized in Section 4.4.

The CTYs from Figure 4.3 were normalized and plotted in Figure 4.4. The catalysts supported on untreated CNT show an increase in activity in the first few hours before the activity decreases, whereas the catalysts supported on GPO treated supports show immediate deactivation. The initial increase can be ascribed to cobalt carbide formation during the reduction which is converted into metallic cobalt in the presence of syngas [77]. It should be noted that the reaction products of all reactors are not measured simultaneously but one after another where each measurement takes about 10 minutes.

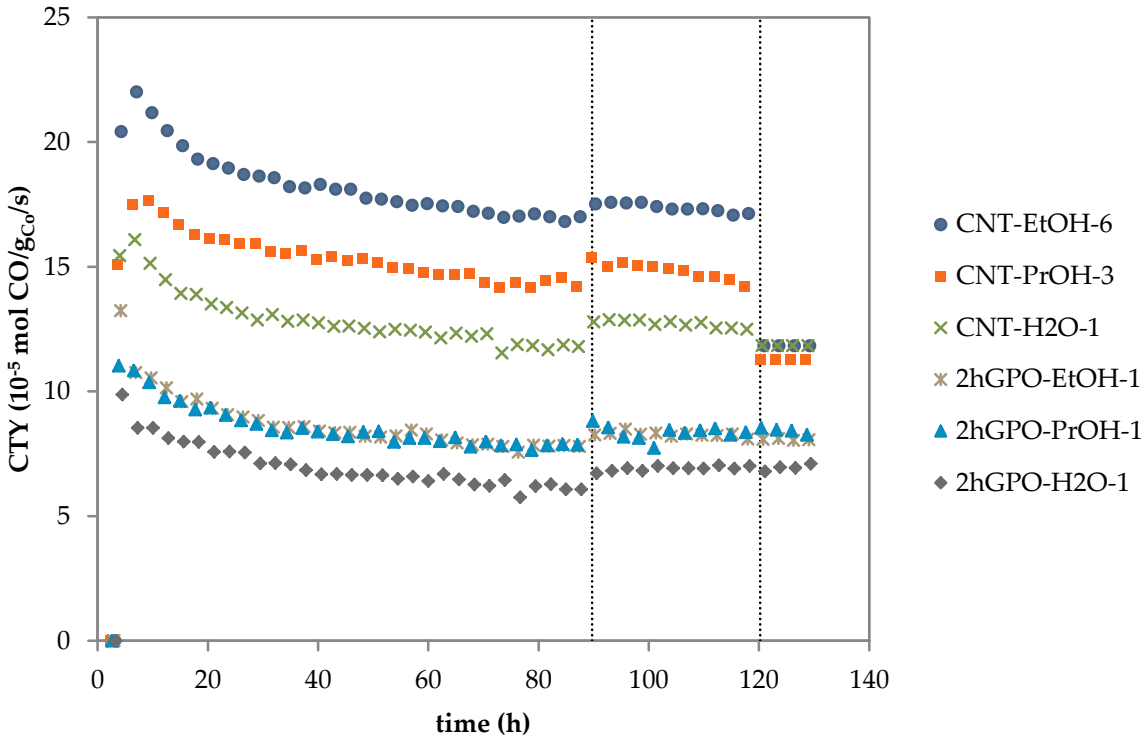

Figure 4.3 Activity of catalysts tested at 20 bar pressure and a temperature of 220 °C, run 3. The GHSV was changed from 4000 h^{-1} to 1875 h^{-1} at 89.7 h and to 1125 h^{-1} at 120.2 h.

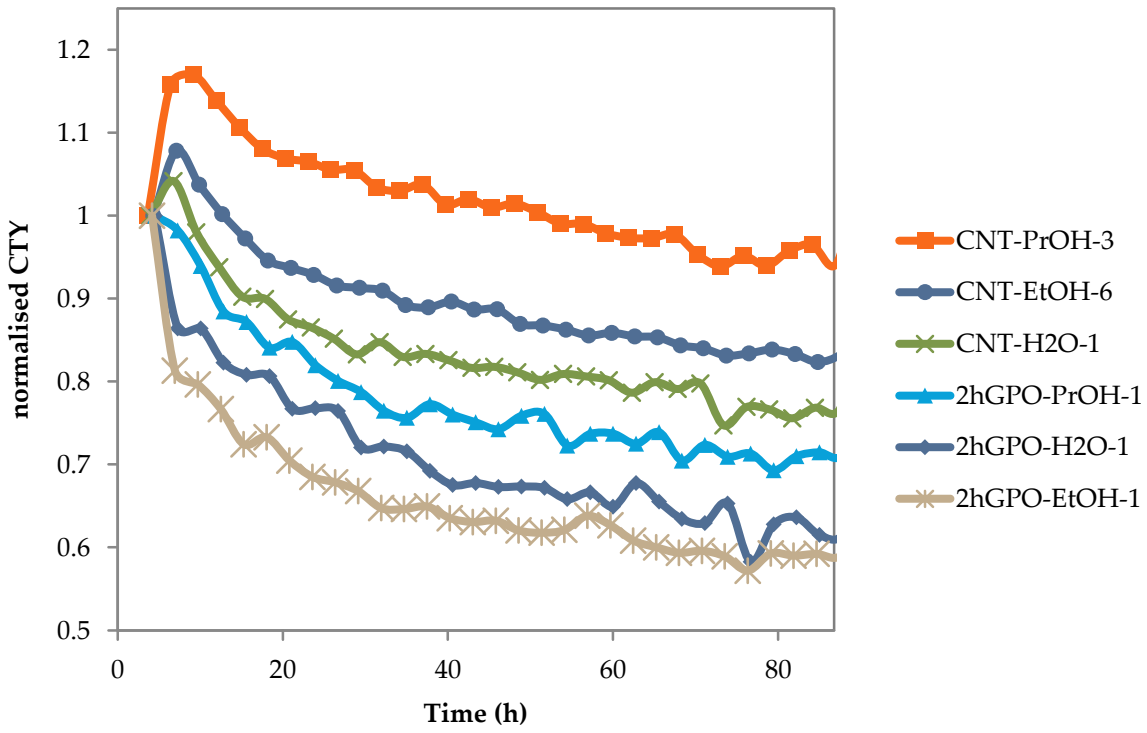

Figure 4.4 Normalized data from Figure 4.3.

4.3.4 Deactivation

In run 4, the catalysts were treated with diluted hydrogen after about 173 h time on stream. The activity is plotted in Figure 4.5. Before the hydrogen treatment, the same trend is observed as seen before where catalysts supported on untreated CNT perform better than those on GPO treated CNT. After the hydrogen treatment, the initial activity is restored for the untreated CNT supported catalysts (which was expected from [44]) whereas the catalysts supported on GPO treated CNT show an activity that is enhanced significantly. An explanation for this might be found in the removal of oxygen atoms from the catalyst that lower the activity, either by oxidizing the cobalt or by electronic effects. From the fact that the activity is restored after the hydrogen treatment for the catalysts supported on untreated CNT, it is concluded that the deactivation mechanism is reversible, i.e. the metal particles do not grow. Reversible deactivation mechanisms are described elsewhere [44] and include pore filling with long-chain waxes limiting accessibility, poisoning and carbidization.

Increasing the reaction temperature might induce particle growth. For catalyst 2hGPO-PrOH-2 it is seen that the initial steady state activity is recovered after increasing the reactor temperature from 220 °C to 250 °C in steps of 10 °C and back to 220 °C, whereas for catalyst CNT-PrOH-3, it is seen that the steady state activity is not recovered after the temperature program. After the hydrogen treatment, the 2hGPO-PrOH-2 sample that has received the temperature program shows an activity that is only slightly lower than the 2hGPO-PrOH-2 sample for which the reactor temperature remained at 220 °C before the hydrogen treatment. However, for catalyst CNT-PrOH-3 after the hydrogen treatment, the sample for which the temperature was varied showed an activity that was significantly lower from the sample that was kept at 220 °C. Catalyst CNT-PrOH-3 is thus irreversibly deactivated at the elevated temperatures, by particle growth. From this it is concluded that the cobalt particles on untreated CNT are more mobile than cobalt particles on GPO treated CNT.

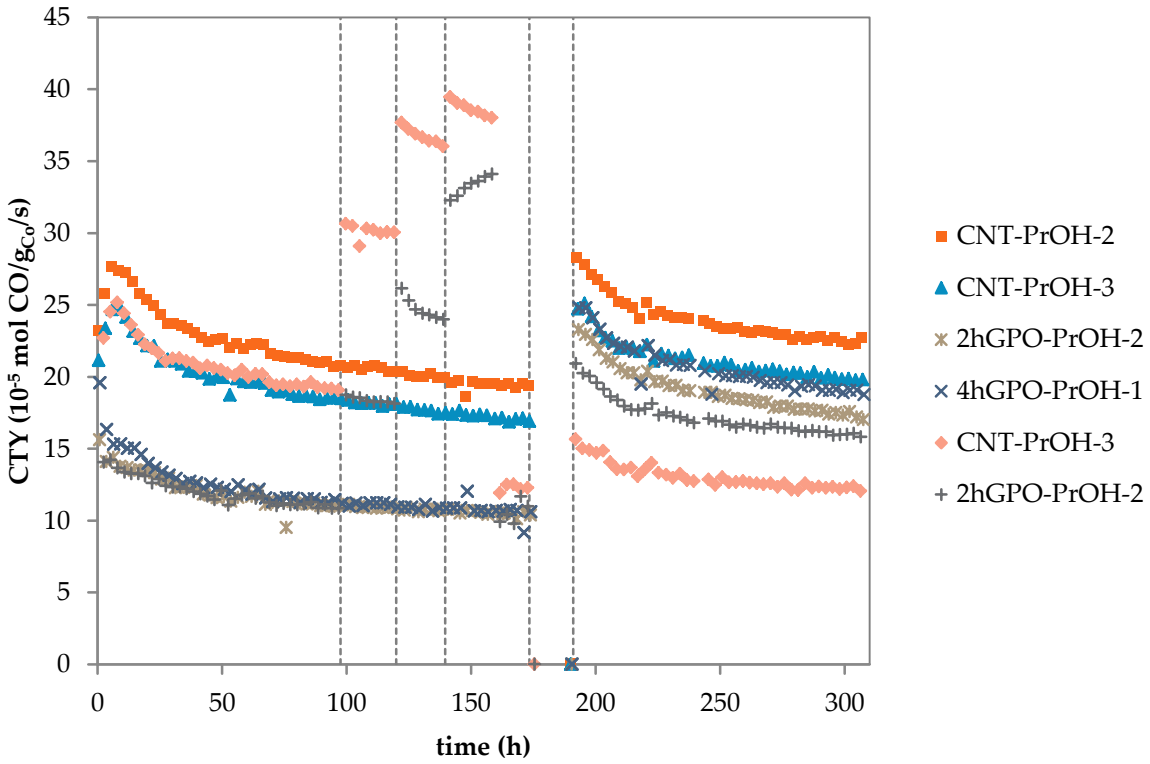

Figure 4.5 Activity of catalysts tested at 20 bar pressure and a temperature of 220 °C, run 4. For two samples the temperature was increased from 220 °C to 250 °C in steps of 10 °C after 97.5 h, 119.9 h and 139.5 h time on stream, respectively, and lowered to 220 °C after 159.4 h time on stream. The hydrogen treatment was started at 173.3 h time on stream.

The presence of oxygen groups on the support surface have a negative influence on the activity of Co on GPO treated CNT catalysts. Co on GPO treated CNT can deactivate by oxidation by the oxygen groups on the support surface. Therefore, the density of oxygen groups on the support surface decreases. The hydrogen treatment reduces the cobalt oxide to cobalt thus removing oxygen atoms from the system.

4.3.5 Product distribution

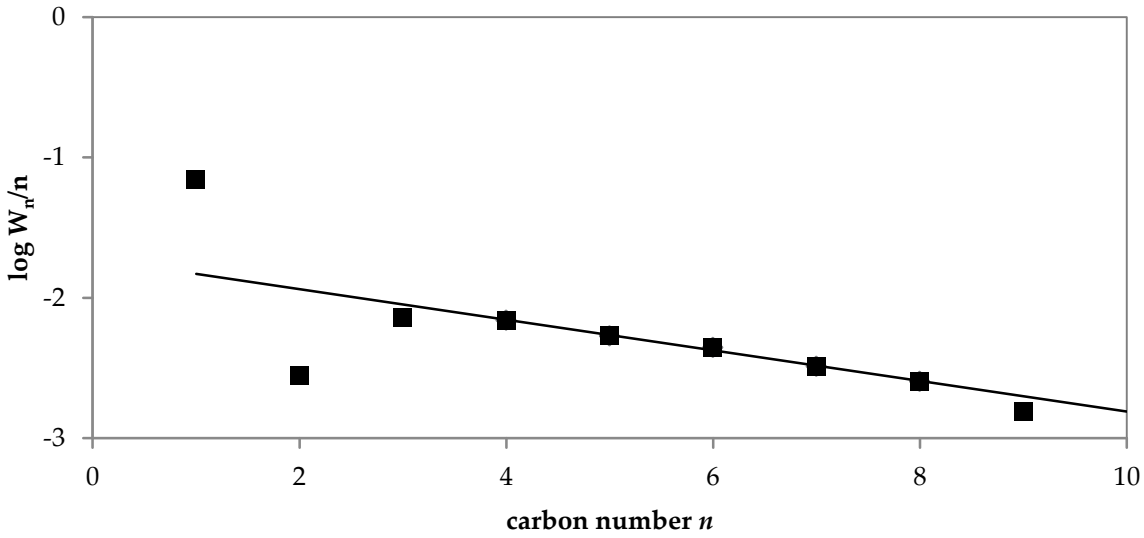

Figure 4.6 ASF plot for catalyst CNT-PrOH-3, measured at 220 °C at 20 bar pressure, H_2:CO=2, GHSV=2000 h^{-1}. A linear fit was applied in the range [4,8] and resulted in R^2=0.9953, α=0.78.

Figure 4.6 shows a typical ASF plot. In this plot, C_1 and C_2 deviate from ideal behavior. First, the C_1 W_n/n is higher than expected from the ASF equation (Equation (1.5)). Considering a methylene unit (CH_2) bound to the catalyst surface, the unit can be attacked by either another methylene unit or by a hydrogen molecule, the latter being more likely to occur resulting in a higher C_1 selectivity. Second, the C_2 W_n/n is lower than expected. When α-olefins are coordinated to the metal, the olefins can grow or terminate. Ethene is a special case: it has two sides that can be attacked whereas longer α-olefins have one side with strong steric hindrance. Because of this, ethene is readily converted to longer chains resulting in a lower C_2 selectivity [1], [78], [79]. This deviation from theoretical ASF behavior enables fitting in the linear range from n=4 onwards. In the high pressure tests, hydrocarbons up to a length of 9 were analyzed individually with condensation effects present for the longer molecules resulting in less reliable results for hydrocarbons with length 8 and 9, thus the linear fit was applied in the range [4,7].

The hydrogen treatment performed in run 4 increased the activity of the catalysts supported on GPO treated CNT. With this increasing activity and increased CO conversion, the C_{5+} selectivity also increased. This was also noticed in run 3: when the GHSV was lowered, the CO conversion increased while the CTY and TOF showed no significant change, but the C_{5+} selectivity did show an increase of about 2 percentage points.

4.3.6 Activation energy

The Arrhenius plot is shown in Figure 4.7. The shown data points were averaged over five measurements after 80, 105, 122 and 144 h run time (run 4) for temperatures of 220, 230, 240 and 250 °C, respectively. A linear fit was applied on the measurements obtained at tempera-

tures of 220, 230 and 240 °C (rightmost three in the graph) for both catalysts. The activation energies were 119 and 112 kJ/mol for CNT-PrOH-3 and 2hGPO-PrOH-2, respectively. The data points at *T*=250 °C were omitted because their reliability was lower as a result of high CO conversion (90% for catalyst CNT-PrOH-3). The activation energies found were of the same order of magnitude as earlier research has shown [56], [80]. The difference between the activation energies of the two systems is not significant. The activation energy is affected by diffusion limitations and it has been shown before that the presence of diffusion limitation lowers the activation energy from 120 kJ/mol to 60–70 kJ/mol [81]. It is therefore concluded that diffusion limitation effects are not present.

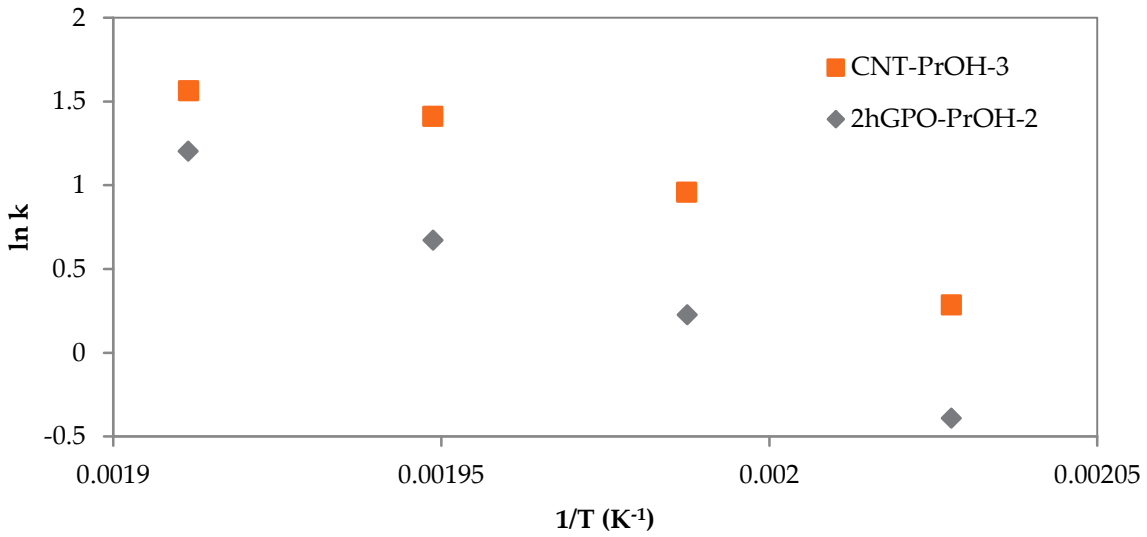

Figure 4.7 Arrhenius plot for catalysts CNT-PrOH-3 and 2hGPO-PrOH-2, run 4.

4.4 Characterization of spent catalysts

TEM images of high pressure spent catalysts were recorded in bright field mode using the method described in Section 2.2.3 and a selection is shown in Figures 4.8–4.13.

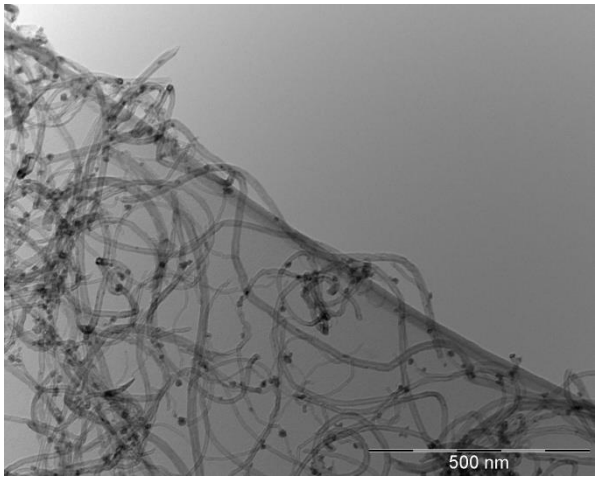

Figure 4.8 TEM image of high pressure spent catalyst CNT-PrOH-3. The image partially shows a hole in the carbon film on the copper grid. Figure 3.4 shows the fresh catalyst.

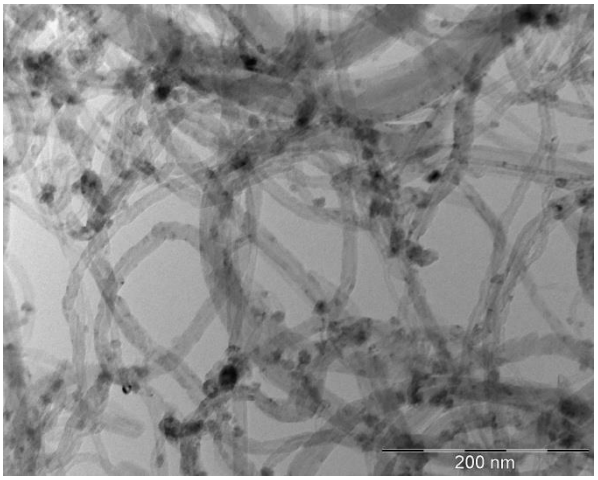

Figure 4.9 TEM image of high pressure spent catalyst 2hGPO-PrOH-2. Figure 3.5 shows the fresh catalyst.

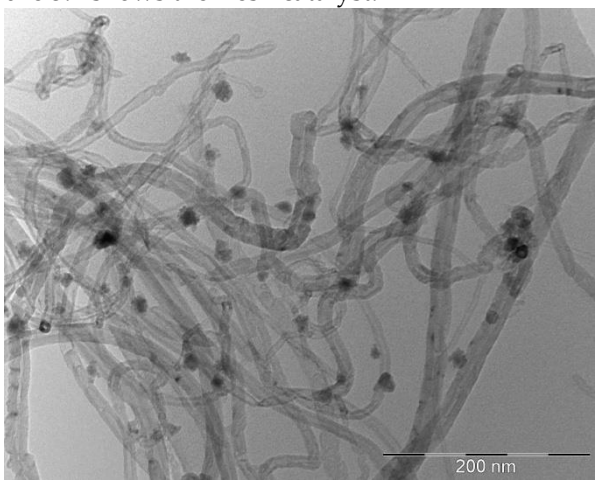

Figure 4.10 TEM image of high pressure spent catalyst CNT-EtOH-6. Figure 3.6 shows the fresh catalyst.

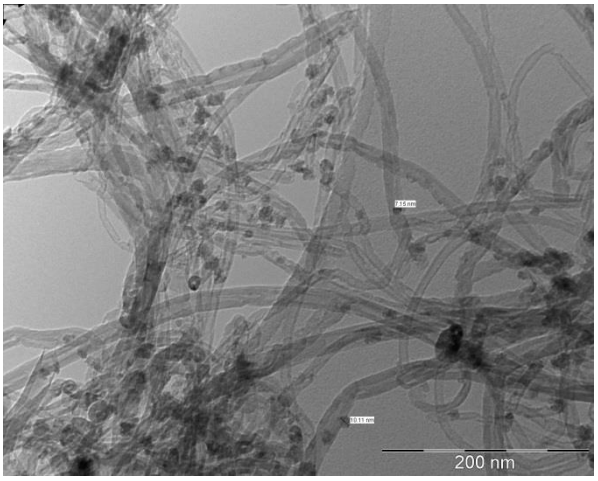

Figure 4.11 TEM image of high pressure spent catalyst 2hGPO-EtOH-1. Figure 3.7 shows the fresh catalyst.

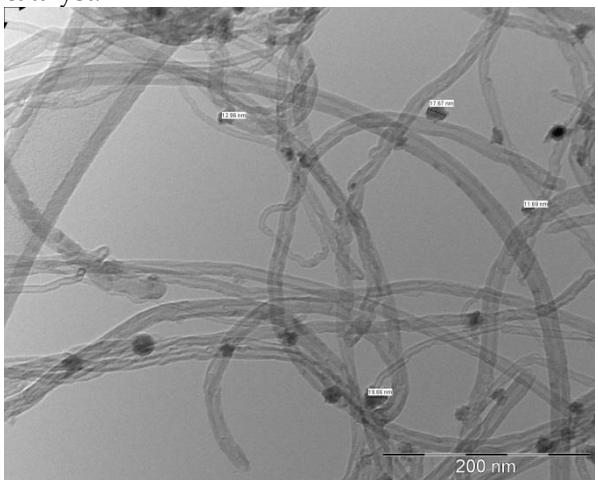

Figure 4.12 TEM image of high pressure spent catalyst CNT-H2O-1. Figure 3.8 shows the fresh catalyst.

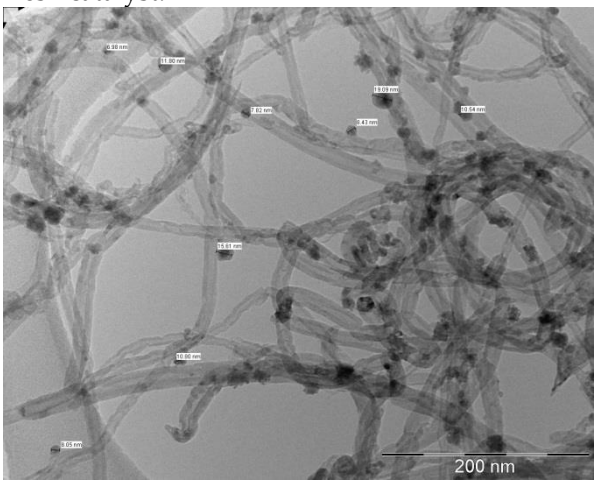

Figure 4.13 TEM image of high pressure spent catalyst 2hGPO-H2O-1. Figure 3.9 shows the fresh catalyst.

Table 4.4 Average Co_3O_4 particle sizes $\langle d \rangle$ (nm) of fresh and spent catalysts and standard deviation σ, as determined by manual analysis of TEM images using iTEM software. The Co equivalent particle sizes were calculated by applying Equation (3.5). The spent catalysts analyzed were tested at high pressure before TEM imaging unless stated otherwise.

	fresh				spent			
	Co_3O_4		Co		Co_3O_4		Co	
catalyst	$\langle d \rangle$	σ	$\langle d \rangle$	σ	$\langle d \rangle$	σ	$\langle d \rangle$	σ
0.5hGPO-PrOH-1[a]					5.9	1.5	4.4	1.1
CNT-PrOH-3					5.4	4.4	4.1	3.3
2hGPO-PrOH-2	4.4	1.0	3.3	0.7				
CNT-H2O-1					13.4	3.4	10.1	2.6
2hGPO-EtOH-1	5.2	1.4	3.9	1.1	9.7	1.4	7.3	1.1
CNT-EtOH-6	5.1	1.5	3.8	1.1	9.3	3.0	7.0	2.3
2hGPO-H2O-1	5.7	1.3	4.3	1.0	10.3	3.1	7.7	2.4

[a] spent at ambient pressure

From the TEM particle size analysis (Table 4.4) it is seen that the metal particles have grown after the reaction. As stated in Section 3.3.2, the particle size does not differ much between the different preparation methods. However, it was also shown that the particle distribution is in fact different depending on the catalyst preparation method. Catalyst CNT-H2O-1 showed clustered particles whereas the particles of the other catalysts were well-distributed. This was especially the case for the catalysts where alcohols were used as impregnation solvent. As seen from the TEM particle size analysis, the particle growth during reduction and reaction is most severe for catalyst CNT-H2O-1. It should also be noted that spent catalysts 0.5hGPO-PrOH-1 and CNT-PrOH-3 have a cobalt particle size below 6 nm, meaning particle size effects limit the activity per surface cobalt atom, illustrated in Figure 4.14.

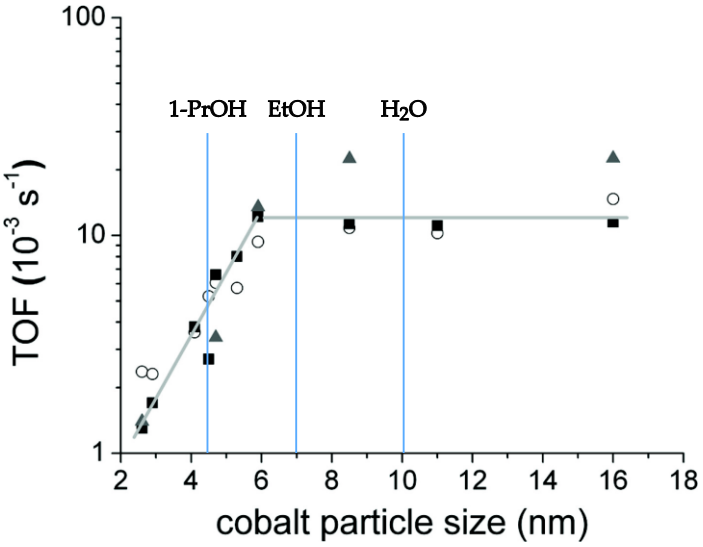

Figure 4.14 Dependency of the TOF on the cobalt particle size [69]. The cobalt particle sizes of spent catalysts CNT-PrOH-3, CNT-EtOH-6 and CNT-H2O-1 are indicated as 1-PrOH, EtOH and H_2O, respectively, for comparison.

4.5 Summary and outlook

The catalysts prepared in Chapter 3 were tested at both ambient and high (20 bar) pressure. In the high pressure tests, the catalysts performed different between runs and therefore the comparisons made are within single runs. The catalysts showed high performance in terms of CTY and apparent TOF, both at ambient and high pressure. Based on the activation energies, it was concluded that diffusion limitations were absent.

It was shown that catalysts supported on untreated CNT have superior performance compared to those on GPO treated CNT. This difference was observed in both pressure regimes, although it was less pronounced in the ambient pressure tests. Catalysts supported on reduced GPO treated CNT suggested an intermediate performance, but this was not confirmed by a second test.

The alcohol (EtOH and 1-PrOH) impregnated catalysts had higher performance than water impregnated catalysts. This was the case for catalysts on both untreated CNT and GPO treated CNT. An explanation for this behavior was found in the particle distribution. Catalysts for which water was used as the impregnation solvent showed more agglomerated particles, which are more likely to grow during the reduction step causing a loss in metallic surface area. For the untreated CNT, a difference was found between the performances of an ethanol impregnated catalyst and a 1-propanol impregnated catalyst: the ethanol impregnated catalyst performed higher. While for most catalysts the cobalt crystallite size had increased after the reaction, the spent 1-propanol catalyst had an equivalent Co crystallite size below 6 nm, and thus in a size range for which the crystallite size highly influences the catalytic activity.

The catalysts supported on untreated CNT showed an interesting activation behavior in the first hours on stream. Similar patterns have been found before for carbidic species. Carbidic cobalt is not active as an FT catalyst but is converted to metallic cobalt by syngas, thereby showing an increase in FTS activity in the first hours on stream.

Increase of temperature leads to faster deactivation for Co on untreated CNT catalysts, whereas the same temperature increase does not deactivate the Co on GPO treated CNT catalysts. The deactivation by the increased temperature was found to be irreversible for the catalyst supported on untreated CNT.

The initial activity was restored by a hydrogen treatment after testing at 220 °C for Co on untreated CNT catalysts, and for the Co on GPO treated CNT catalysts the activity is even higher than the initial activity. Furthermore, the latter showed a lower deactivation rate.

The growth catalyst of the CNT did not have an influence on the activity nor on the selectivity of the catalysts.

The increase in activity found for the catalysts on untreated CNT during the first hours on stream was attributed to carbidic cobalt that is converted to metallic cobalt by syngas. Further research is necessary to confirm this. An *in situ* XRD test might bring this evidence.

Chapter 5

Summary and outlook

In this work, different CNT supported cobalt catalysts for the Fischer-Tropsch synthesis were prepared and investigated. The supports that were used are untreated CNT, CNT that were pre-treated with nitric acid vapor (gas phase oxidation or GPO, introducing oxygen containing groups on the CNT surface) and GPO treated CNT that were reduced by hydrogen. The GPO treated CNT had a rougher surface than the untreated CNT. Both untreated CNT and GPO treated CNT were thermally highly stable. The acidity of the GPO treated CNT was investigated by acid-base titrations and it was found that the acid group content increases in the first two hours of GPO treatment and then stabilizes at about 0.45 mmol/g.

All catalysts were prepared by incipient wetness impregnation using $Co(NO_3)_2 \cdot 6H_2O$ as metal precursor, dissolved in either 1-propanol, ethanol or water. After impregnation, the samples were dried at a temperature 20 K below the boiling point of the solvent (i.e. 60 °C for ethanol and 80 °C for 1-propanol and water) in flowing nitrogen and thermally treated at 250 °C in flowing nitrogen. The obtained catalysts had cobalt-equivalent particle sizes of 3-4 nm (determined by TEM) and the ethanol and 1-propanol impregnated catalysts were highly dispersed, whereas the water impregnated catalysts showed agglomerated particles. This was explained by means of wetting. The reduction behavior was investigated by a temperature programmed reduction experiment. The TPR patterns of Co/CNT catalysts were different from Co supported on oxidic supports: an extra peak was seen which could not be assigned to the reduction of cobalt but instead to a reaction between the CNT and hydrogen. Furthermore, the reduction peaks of cobalt oxide supported on GPO treated CNT have shifted to higher temperatures compared to cobalt oxide supported on untreated CNT.

The catalysts were tested catalytically for the Fischer-Tropsch synthesis at ambient and high (20 bar) pressure. It was found that the support surface pre-treatment has severe impact on catalytic performance. Support pre-treatment with nitric acid vapor lowers catalytic activity at 20 bar syngas pressure by a factor 2 compared to catalysts for which the support has had no pre-treatment. Removal of oxygen groups by thermal treatment in a hydrogen gas suggested an intermediate activity but this was not confirmed by a second test. It can still be concluded that the oxygen groups on the support surface are not beneficial for the activity of the catalysts.

The impregnation solvent also had an influence on the catalytic performance of the catalysts. The alcohol (ethanol and 1-propanol) impregnations result in a higher activity than water impregnation. This was explained by the agglomerated metal particles from the water impregnated samples that have a high chance to combine and form bigger particles, resulting in a loss of metal surface area.

While on stream, all catalysts showed a decreasing activity over time. The initial activity was restored by a hydrogen treatment and it is therefore concluded that the deactivation process is reversible. For the catalysts supported on GPO treated CNT, the activity was even higher than the initial activity. An explanation was found in the oxygen groups on the CNT surface, which are able to oxidize the cobalt particles. By the hydrogen treatment, the cobalt oxide is re-reduced to metallic cobalt and the oxygen atoms are removed from the system. After the treatment, the lower oxygen content results in a higher activity.

By increasing the reactor temperature, it was found that the thermal stability of the catalysts is higher for cobalt supported on GPO treated CNT compared to cobalt on untreated CNT. Therefore it was concluded that the oxygen groups are able to stabilize the cobalt metal particles.

As the reducibility of the catalysts might have an impact on the behavior of the catalysts, it is interesting to further clarify the reducibility. *In situ* XRD was suggested to follow the reduction process. Other interesting options are Extended X-ray Absorption Fine Structure (EXAFS) and X-ray Absorption Near Edge Structure (XANES). Another analysis can be performed by using a mass spectrometer coupled to a temperature programmed reduction setup. This way, the reduction behavior can be related to the products formed during the reduction.

The residence time and surface coverage of reactants can be investigated by Steady State Isotopic Transient Kinetic Analysis (SSITKA), and by using infrared techniques such as polarization modulation reflection absorption infrared spectroscopy (PM-RAIRS) the binding state of CO molecules can be determined.

Acknowledgements

On 12 November 2012 I started my research project at the Inorganic Chemistry and Catalysis group. I have met quite some interesting people which I am very grateful to. To start off, Thomas, as my daily supervisor, thank you for offering me this project and guiding me through the project, including all interesting discussions and ideas, for performing experiments and measurements that I was unable to do (including TEM and TPR) and for proofreading this thesis. Your wide knowledge made me understand more and more in catalysis research. Krijn, your ideas and input have been of great value for me and for this project. Your drive to fully understand the research that is done was very inspiring to me. Harry, thank you for the introduction to the group and ideas and discussion following my research proposal.

Without the help of some people I wouldn't have been able to present the work as it is now. Thank you Hans for the TEM sessions we had. Due to your extensive experience we imaged a large number of samples in a relatively low amount of time, the recorded images being of high quality. Marjan, thank you for performing the TGA measurements and learning me how to operate the x-ray diffractometer. Korneel, thank you for performing some TPR experiments. Arjan,, thank you for doing the chemisorption experiments, and as a fellow FT-er, thank you for your guidance when Thomas was absent.

Last but not least I would like to thank my fellow students for making my time at the ICC group fun. Tom, Tanja, Karst and Thomas, we've spent quite some time together as neighbors on the balcony. Let's hope the Tricolore lunches on Thursdays will become a tradition.

Finally, to all ICC members I haven't named yet, thank you!

All the best!

Wouter Lamme
February 2014

Bibliography

[1] M. E. Dry and A. P. Steynberg, Eds., *Fischer-Tropsch Technology*, vol. 152. Elsevier, 2004.

[2] M. E. Dry, "The Fischer–Tropsch process: 1950–2000," *Catal. Today*, vol. 71, no. 3–4, pp. 227–241, 2002.

[3] H. Schulz, "Short history and present trends of Fischer–Tropsch synthesis," *Appl. Catal. A Gen.*, vol. 186, no. 1, pp. 3–12, 1999.

[4] H. H. Storch, R. B. Anderson, L. J. E. Hofer, C. O. Hawk, H. C. Anderson, and N. Golumbic, "Synthetic liquid fuels from the hydrogenation of carbon monoxide. Part 1. Review of Literature," *United States Bur. Mines Tech. Pap.*, no. 709, 1948.

[5] BP, "Statistical Review of World Energy 2013," 2013.

[6] M. E. Spaght, "The Manufacture and Application of Lubricants in Germany," 1945.

[7] "Zwanzig Minuten Kohlenklau," *Der Spiegel*, no. 49, p. 6, 1947.

[8] R. B. Anderson, *The Fischer-Tropsch Synthesis*. Orlando: Academic Press, Inc., 1984.

[9] F. D'Olier, H. C. Alexander, G. W. Ball, H. L. Bowman, J. K. Galbraith, R. Likert, F. A. McNamee, P. H. Nitze, R. P. Russell, F. Searls Jr., T. P. Wright, and C. C. Cabot, "United States Strategic Bombing Survey: Summary Report (European War)," Washington, 1945.

[10] M. E. Dry, "Practical and theoretical aspects of the catalytic Fischer-Tropsch process," *Appl. Catal. A Gen.*, vol. 138, no. 2, pp. 319–344, 1996.

[11] Elsevier B.V., "Scopus analyze results - TITLE-ABS-KEY(Fischer-Tropsch)." [Online]. Available: http://www.scopus.com/term/analyzer.url. [Accessed: 08-Oct-2013].

[12] A. E. Kramer, "Gazprom shuts off gas links to Ukraine," *The New York Times*, 2009.

[13] "Kolen en kolenproducten; winning, in- en uitvoer, productie; vanaf 1900," *CBS Statline*. [Online]. Available: http://statline.cbs.nl/StatWeb/publication/?VW=T&DM=SLNL&PA=71554ned&D1=a&D2=0,2,10,20,30,40,50,60,70,80,85,90,95,(l-1),l&HD=140212-2001&HDR=T&STB=G1. [Accessed: 12-Feb-2014].

[14] "The Rise and Fall of Germany's Coal Mining Industry," *DW*, 2007. [Online]. Available: http://dw.de/p/9mXZ. [Accessed: 12-Feb-2014].

[15] A. van Wijck, "Mobiele afvalvergasser voor leger," *Technisch Weekblad*, p. 1, 06-Sep-2013.

[16] O. P. R. van Vliet, A. P. C. Faaij, and W. C. Turkenburg, "Fischer–Tropsch diesel production in a well-to-wheel perspective: A carbon, energy flow and cost analysis," *Energy Convers. Manag.*, vol. 50, no. 4, pp. 855–876, 2009.

[17] "GGFR Partners Unlock Value of Wasted Gas," *Sustainable Development - World Bank*, 2009. [Online]. Available: http://go.worldbank.org/ESORQZPSJ0. [Accessed: 13-Feb-2014].

[18] Bureau of Labor Statistics, "CPI Inflation Calculator," 2013. [Online]. Available: http://www.bls.gov/data/inflation_calculator.htm. [Accessed: 30-Sep-2013].

[19] L. Dong, S. Wei, S. Tan, and H. Zhang, "GTL or LNG: which is the best way to monetize 'stranded' natural gas?," *Pet. Sci.*, vol. 5, no. 4, pp. 388–394, 2008.

[20] C. Song and X. Ma, "New design approaches to ultra-clean diesel fuels by deep desulfurization and deep dearomatization," *Appl. Catal. B Environ.*, vol. 41, no. 1, pp. 207–238, 2003.

[21] M. E. Dry, "Fischer–Tropsch reactions and the environment," *Appl. Catal. A Gen.*, vol. 189, no. 2, pp. 185–190, 1999.

[22] J. G. Speight, *Handbook of petroleum product analysis*. Hoboken, NJ, USA: John Wiley & Sons, 2002.

[23] J. Szybist, S. Kirby, and A. Boehman, "NOx emissions of alternative diesel fuels: A comparative analysis of biodiesel and FT diesel," *Energy & fuels*, no. 19, pp. 1484–1492, 2005.
[24] Shell Global, "Pearl GTL - an overview." [Online]. Available: http://www.shell.com/global/aboutshell/major-projects-2/pearl/overview.html. [Accessed: 07-Oct-2013].
[25] "Sasol's world-scale ethane cracker & gas-to-liquids facility." Sasol.
[26] C. Krauss, "South African Company to Build U.S. Plant to Convert Gas to Liquid Fuels," *The New York Times*, 03-Dec-2012.
[27] "Natural Gas," *Chevron*, 2013. [Online]. Available: http://www.chevron.com/deliveringenergy/naturalgas/. [Accessed: 13-Feb-2014].
[28] Z. Liu, S. Shi, and Y. Li, "Coal liquefaction technologies—Development in China and challenges in chemical reaction engineering," *Chem. Eng. Sci.*, vol. 65, no. 1, pp. 12–17, 2010.
[29] E. Iglesia, "Design, synthesis, and use of cobalt-based Fischer-Tropsch synthesis catalysts," *Appl. Catal. A Gen.*, vol. 161, no. 1–2, pp. 59–78, 1997.
[30] N. E. Tsakoumis, M. Rønning, Ø. Borg, E. Rytter, and A. Holmen, "Deactivation of cobalt based Fischer–Tropsch catalysts: A review," *Catal. Today*, vol. 154, no. 3–4, pp. 162–182, 2010.
[31] A. M. Saib, D. J. Moodley, I. M. Ciobîcă, M. M. Hauman, B. H. Sigwebela, C. J. Weststrate, J. W. Niemantsverdriet, and J. van de Loosdrecht, "Fundamental understanding of deactivation and regeneration of cobalt Fischer–Tropsch synthesis catalysts," *Catal. Today*, vol. 154, no. 3–4, pp. 271–282, 2010.
[32] P. K. Agrawal, J. R. Katzer, and W. H. Manogue, "Methanation over Transition Metal Catalysts," *J. Catal.*, vol. 69, pp. 327–344, 1981.
[33] H. M. Torres Galvis, J. H. Bitter, C. B. Khare, M. Ruitenbeek, a I. Dugulan, and K. P. de Jong, "Supported iron nanoparticles as catalysts for sustainable production of lower olefins.," *Science*, vol. 335, no. 6070, pp. 835–8, 2012.
[34] M. Bowker, "The going rate for catalysis," *Nat. Mater.*, vol. 1, pp. 205–206, 2002.
[35] G. L. Bezemer, T. J. Remans, A. P. van Bavel, and A. I. Dugulan, "Direct evidence of water-assisted sintering of cobalt on carbon nanofiber catalysts during simulated Fischer-Tropsch conditions revealed with in situ mossbauer spectroscopy.," *J. Am. Chem. Soc.*, vol. 132, no. 25, pp. 8540–1, 2010.
[36] J. A. Moulijn, A. E. Van Diepen, and F. Kapteijn, "Catalyst deactivation: is it predictable? What to do?," *Appl. Catal. A Gen.*, vol. 212, pp. 3–16, 2001.
[37] W. M. Haynes, Ed., *Handbook of Chemistry and Physics*, 93rd ed. Boca Raton: CRC Press, 2012.
[38] F. G. Botes, J. W. Niemantsverdriet, and J. van de Loosdrecht, "A comparison of cobalt and iron based slurry phase Fischer–Tropsch synthesis," *Catal. Today*, vol. 215, pp. 112–120, 2013.
[39] P. L. Spath and D. C. Dayton, "Preliminary Screening — Technical and Economic Assessment of Synthesis Gas to Fuels and Chemicals with Emphasis on the Potential for Biomass-Derived Syngas," Golden, CO, USA, 2003.
[40] S. Iijima, "Helical microtubules of graphitic carbon," *Nature*, vol. 354, no. 6348, pp. 56–58, 1991.
[41] M. Cadek, O. Vostrowsky, and A. Hirsch, "Carbon, 7. Fullerenes and Carbon Nanomaterials," *Ullmann's Encycl. Ind. Chem.*, pp. 23–44, 2012.
[42] J.-P. Tessonnier, M. Becker, W. Xia, F. Girgsdies, R. Blume, L. Yao, D. S. Su, M. Muhler, and R. Schlögl, "Spinel-Type Cobalt-Manganese-Based Mixed Oxide as Sacrificial Catalyst for the High-Yield Production of Homogeneous Carbon Nanotubes," *ChemCatChem*, vol. 2, no. 12, pp. 1559–1561, 2010.
[43] P. Serp, M. Corrias, and P. Kalck, "Carbon nanotubes and nanofibers in catalysis," *Appl. Catal. A Gen.*, vol. 253, no. 2, pp. 337–358, 2003.
[44] Z. Yu, Ø. Borg, D. Chen, E. Rytter, and A. Holmen, "Role of surface oxygen in the preparation and deactivation of carbon nanofiber supported cobalt Fischer–Tropsch catalysts," *Top. Catal.*, vol. 45, no. 1–4, pp. 69–74, 2007.

[45] M. K. van der Lee, A. J. van Dillen, J. H. Bitter, and K. P. de Jong, "Deposition precipitation for the preparation of carbon nanofiber supported nickel catalysts.," *J. Am. Chem. Soc.*, vol. 127, no. 39, pp. 13573–82, 2005.
[46] G. L. Bezemer, "Cobalt supported on carbon nanofibers as catalysts for the Fischer-Tropsch synthesis," Utrecht University, 2006.
[47] D. S. Su, S. Perathoner, and G. Centi, "Nanocarbons for the Development of Advanced Catalysts.," *Chem. Rev.*, 2013.
[48] R. W. Gosselink, R. van den Berg, W. Xia, M. Muhler, K. P. de Jong, and J. H. Bitter, "Gas phase oxidation as a tool to introduce oxygen containing groups on metal-loaded carbon nanofibers," *Carbon*, vol. 50, no. 12, pp. 4424–4431, 2012.
[49] V. Likodimos, T. a. Steriotis, S. K. Papageorgiou, G. E. Romanos, R. R. N. Marques, R. P. Rocha, J. L. Faria, M. F. R. Pereira, J. L. Figueiredo, A. M. T. Silva, and P. Falaras, "Controlled surface functionalization of multiwall carbon nanotubes by HNO3 hydrothermal oxidation," *Carbon*, vol. 69, pp. 311–326, 2014.
[50] M. Park, B.-H. Kim, S. Kim, D.-S. Han, G. Kim, and K.-R. Lee, "Improved binding between copper and carbon nanotubes in a composite using oxygen-containing functional groups," *Carbon*, vol. 49, no. 3, pp. 811–818, 2011.
[51] K. Balasubramanian and M. Burghard, "Chemically functionalized carbon nanotubes.," *Small*, vol. 1, no. 2, pp. 180–92, 2005.
[52] W. Xia, C. Jin, S. Kundu, and M. Muhler, "A highly efficient gas-phase route for the oxygen functionalization of carbon nanotubes based on nitric acid vapor," *Carbon*, vol. 47, no. 3, pp. 919–922, 2009.
[53] T. O. Eschemann, "Proposal Wouter Lamme." 2012.
[54] R. Abolfath and K. Cho, "Computational studies for reduced graphene oxide in hydrogen-rich environment," *J. Phys. Chem. A*, vol. 116, p. 1820, 2012.
[55] "Wolfram|Alpha Knowledgebase," 2013. [Online]. Available: http://www.wolframalpha.com.
[56] R. Manchester, "Study on the preparation of Highly Active and Stable Cobalt on Carbon Nanotubes Catalysts for the Fischer-Tropsch reaction," Utrecht University, 2012.
[57] K. A. Wepasnick, B. A. Smith, J. L. Bitter, and D. Howard Fairbrother, "Chemical and structural characterization of carbon nanotube surfaces.," *Anal. Bioanal. Chem.*, vol. 396, no. 3, pp. 1003–14, 2010.
[58] K. P. de Jong, *Synthesis of Solid Catalysts*. Weinheim: WILEY-VCH Verlag GmbH & Co., 2009.
[59] A. Neimark, "Theory of preparation of supported catalysts," *Ind. Eng. Chem. Prod. Res. Dev.*, pp. 439–450, 1981.
[60] "Baytubes C 150 P Product Datasheet." Bayer MaterialScience AG, Leverkusen, 2010.
[61] T. W. van Deelen, "Niobia-Promoted Co/CNT Catalysts for the Fischer-Tropsch Synthesis," Utrecht University, 2014.
[62] C. Ehrhardt, M. Gjikaj, and W. Brockner, "Thermal decomposition of cobalt nitrato compounds: Preparation of anhydrous cobalt(II)nitrate and its characterisation by Infrared and Raman spectra," *Thermochim. Acta*, vol. 432, no. 1, pp. 36–40, 2005.
[63] H.-Y. Lin and Y.-W. Chen, "The mechanism of reduction of cobalt by hydrogen," *Mater. Chem. Phys.*, vol. 85, no. 1, pp. 171–175, 2004.
[64] P. Scherrer, "Bestimmung der Grösse und der inneren Struktur von Kolloidteilchen mittels Röntgenstrahlen," *Nachrichten von der Gesellschaft der Wissenschaften zu Göttingen*, pp. 98–100, 1918.
[65] D. Schanke, S. Vada, E. Blekkan, A. Hilmen, A. Hoff, and A. Holmen, "Study of Pt-promoted cobalt CO hydrogenation catalysts," *J. Catal.*, vol. 156, pp. 85–95, 1995.
[66] R. C. Reuel and C. H. Bartholomew, "The Stoichiometries of H2 and CO Adsorptions on Cobalt: Effects of Support and Preparation," *J. Catal.*, vol. 85, pp. 63–77, 1984.
[67] S. J. Tauster, S. C. Fung, R. T. Baker, and J. A. Horsley, "Strong interactions in supported-metal catalysts," *Science*, vol. 211, no. 4487, pp. 1121–5, 1981.

[68] Z. Yu, Ø. Borg, D. Chen, B. C. Enger, V. Frøseth, E. Rytter, H. Wigum, and A. Holmen, "Carbon Nanofiber Supported Cobalt Catalysts for Fischer–Tropsch Synthesis with High Activity and Selectivity," *Catal. Letters*, vol. 109, no. 1–2, pp. 43–47, 2006.
[69] J. P. den Breejen, "Cobalt particle size effects in catalysis," Utrecht University, 2010.
[70] H. Xiong, M. A. M. Motchelaho, M. Moyo, L. L. Jewell, and N. J. Coville, "Correlating the preparation and performance of cobalt catalysts supported on carbon nanotubes and carbon spheres in the Fischer–Tropsch synthesis," *J. Catal.*, vol. 278, no. 1, pp. 26–40, 2011.
[71] G. Jacobs, Y. Ji, B. H. Davis, D. Cronauer, A. J. Kropf, and C. L. Marshall, "Fischer–Tropsch synthesis: Temperature programmed EXAFS/XANES investigation of the influence of support type, cobalt loading, and noble metal promoter addition to the reduction behavior of cobalt oxide particles," *Appl. Catal. A Gen.*, vol. 333, no. 2, pp. 177–191, 2007.
[72] A. Jess and P. Wasserscheid, *Chemical Technology: An Integral Textbook (Google eBook)*. John Wiley & Sons, 2013.
[73] G. Rothenberg, *Catalysis*. Weinheim: WILEY-VCH Verlag GmbH & Co., 2008.
[74] T. O. Eschemann, J. H. Bitter, and K. P. de Jong, "Effects of loading and synthesis method of titania-supported cobalt catalysts for Fischer–Tropsch synthesis," *Catal. Today*, 2013.
[75] J. H. den Otter and K. P. de Jong, "Highly Selective and Active Niobia-Supported Cobalt Catalysts for Fischer–Tropsch Synthesis," *Top. Catal.*, 2013.
[76] R. van Hardeveld and F. Hartog, "The statistics of surface atoms and surface sites on metal crystals," *Surf. Sci.*, vol. 15, pp. 189–230, 1969.
[77] J. Mohandas, M. Gnanamani, and G. Jacobs, "Fischer–Tropsch Synthesis: Characterization and Reaction Testing of Cobalt Carbide," *ACS Catal.*, no. 1, pp. 1581–1588, 2011.
[78] G. Henrici-Olivé and S. Olivé, "The Fischer-Tropsch Synthesis: Molecular Weight Distribution of Primary Products and Reaction Mechanism," *Angew. Chemie Int. Ed. English*, vol. 15, no. 3, pp. 136–141, 1976.
[79] I. Puskas and R. Hurlbut, "Comments about the causes of deviations from the Anderson–Schulz–Flory distribution of the Fischer–Tropsch reaction products," *Catal. Today*, vol. 84, no. 1–2, pp. 99–109, 2003.
[80] J. Thiessen, A. Rose, J. Meyer, A. Jess, and D. Curulla-Ferré, "Effects of manganese and reduction promoters on carbon nanotube supported cobalt catalysts in Fischer–Tropsch synthesis," *Microporous Mesoporous Mater.*, vol. 164, pp. 199–206, 2012.
[81] M. Post, A. C. van 't Hoog, J. Minderhoud, and S. Sie, "Diffusion Limitations in Fischer-Tropsch Catalysts," *AIChE J.*, vol. 35, no. 7, p. 1107, 1989.